Author: Visser, Erwin Lourens
Title: Neutrinos from the Milky Way
Issue Date: 2015-05-12

5

CONSTRAINTS ON THE DIFFUSE GALACTIC NEUTRINO FLUX FROM ANTARES

Now that the signal flux has been described, and the detector used to perform a measurement of this flux is introduced, the stage is set to describe the analysis of the ANTARES data. This is the main focus of this chapter. The obtained results are also shown and discussed.

The analysis consists of comparing the number of events from the *on-source* region, with the number of events from the *off-source* region. The on-source region, also called the *signal region*, is a rectangular area encompassing the Galactic plane, where the highest signal is expected. The optimal size of the signal region depends on the angular distribution of the diffuse Galactic neutrino flux. The statistical tools used to determine this optimal size are described in section 5.1.

The off-source region will consist of a number of regions (also called *background regions*), which have the same size and detector coverage as the signal region, but are centred on directions where the expected signal is low. The background regions are constructed in such a way that the number of background events expected in each of them is the same as that expected in the signal region. The method used to construct these background regions is also described in section 5.1.

After the signal and background regions are defined, it has been verified that the background regions are equivalent. The checks that have been performed are described in section 5.2. The data are also compared to the predictions from a MC simulation for events coming from these background regions. A reasonable agreement between data and MC is required, since the MC is used to optimise the cut values of the variables introduced in the previous chapter (Λ, β, E_{rec} and R_{GF}) and to convert the measured number of events into a flux limit.

The cut variables are used to create a final event sample with a high purity. The background (atmospheric muons and atmospheric neutrinos) should then be reduced as much as possible. The same statistical tools as used to determine the optimal size of the signal region are used for this optimisation, which is described in section 5.3.

After the final event sample has been obtained, the sensitivity of ANTARES to the diffuse Galactic neutrino flux can be determined. This is explained in section 5.4, and a comparison is presented with the sensitivity of the AMANDA-II experiment. The influence of the cosmic neutrino signal measured by IceCube is discussed in more detail in this section as well.

The final step is to count the number of events in the signal region and compare it to the number of events from the background regions. The event numbers are used to set flux limits, which are shown and discussed in section 5.5.

5.1 DETERMINING THE OPTIMAL SIGNAL REGION SIZE

The advantage of using an off-source region to perform a measurement of the background, is that no modelling of the background is required for the analysis. In this way, the analysis is in principle not affected by any systematic uncertainties on the background. A MC simulation is still used to optimise the size of the signal region and the cuts on the quality variables, as well as to estimate the number of signal events expected from the diffuse Galactic neutrino flux. In case the MC simulation does not fully describe the data, this could lead to non-optimal values for the parameters or a wrong estimate of the expected number of signal events. The influence of the MC simulation on the measurement is reduced however, since it is not used to estimate the background.

The goal of the analysis is to produce a flux limit, so the parameters are optimised for the best sensitivity. This is explained in more detail below, together with the statistical tools required for this.

5.1.1 *Statistical tools*

In counting experiments, testing for the presence of a signal is based on the determination of the probability that the observed number of events is caused by fluctuations of the background alone. The probability to measure n_{obs} events when μ_{b} are expected from the background is given by Poisson statistics:

$$P(n_{\text{obs}}|\,\mu_{\text{b}}) = \text{Pois}(n_{\text{obs}}|\,\mu_{\text{b}}) = \frac{\mu_{\text{b}}^{n_{\text{obs}}} e^{-\mu_{\text{b}}}}{n_{\text{obs}}!}, \tag{5.1}$$

where the probability is conditional (i. e. the probability to measure n_{obs} given μ_{b}).

For equation 5.1 it is assumed that the expected number of background events is exactly known (or the uncertainty on it can be neglected). When the expected number of background events has a non-neglible uncertainty, things become more complicated. This is the case when using an off-source region to determine the number of background events from the data. The advantage of not having to rely on any modelling of the background outweighs this additional complexity: the measurement is not affected by systematic errors on the background. This method is therefore commonly used in both astronomy and high-energy physics. In the former, the measurement of the background consists of pointing the telescope in a source-free direction, whereas in the latter so-called *sidebands* are used[27]. In ANTARES, the Fermi bubble analysis [Adrián-Martínez et al., 2014a] has made use of on- and off-source regions.

When the uncertainty on the background is non-neglible, the probability given by equation 5.1 has to be modified to include the additional measurement. This subsidiary measurement can also be described using a Poissonian [Cousins et al., 2008; Li and Ma, 1983], in which n_{bg} events are measured in the off-source region where μ_{bg} are expected. The off-source region does not need to have the same size as the on-source region, and is often chosen to be bigger to reduce the statistical uncertainty on n_{bg}. The ratio of off-source to on-source region is called τ, which is usually known and given by:

$$\tau = \frac{\mu_{\mathrm{bg}}}{\mu_{\mathrm{b}}}. \tag{5.2}$$

Since the two measurements are independent, the probability to measure n_{obs} when $\mu_{\mathrm{obs}}(= \mu_{\mathrm{b}} + \mu_{\mathrm{s}})$ are expected, and n_{bg} events when μ_{bg} are expected, can be written as:

$$P(n_{\mathrm{obs}}, n_{\mathrm{bg}} | \mu_{\mathrm{b}}, \mu_{\mathrm{s}}; \tau) = \mathrm{Pois}(n_{\mathrm{obs}} | \mu_{\mathrm{b}} + \mu_{\mathrm{s}}) \mathrm{Pois}(n_{\mathrm{bg}} | \tau\mu_{\mathrm{b}}), \tag{5.3}$$

where μ_{s} is the expected number of signal events.

After performing a measurement of both n_{bg} and n_{obs}, a confidence interval $[\mu_{\mathrm{low}}, \mu_{\mathrm{up}}]$ can be constructed for μ_{s} at a certain confidence level α (for instance 90%). Using frequentist statistics, this means that the interval contains the fixed unknown value of the number of signal events in a fraction α of the experiments:

$$P(\mu_{\mathrm{s}} \in [\mu_{\mathrm{low}}, \mu_{\mathrm{up}}]) = \alpha. \tag{5.4}$$

Using Bayesian statistics, one rather speaks of a credibility interval, and using a 'confidence' level of α means in this case that the

[27] *A sample of events which is near the signal region in the measured parameter, for instance around an expected mass peak of some hypothesised new particle.*

probability that the true value of the number of signal events is within the interval is α [Metzger, 2002].

If the confidence interval is constructed according to equation 5.4, it is said to *cover* that parameter at the stated confidence level. In case $P(\mu_s \in [\mu_{low}, \mu_{up}]) < \alpha$ the interval is said to undercover the parameter, and when $P(\mu_s \in [\mu_{low}, \mu_{up}]) > \alpha$ it is said to overcover[28]. Although overcoverage is generally considered not to be such a big problem as undercoverage, it is still undesirable since the interval is larger than it should be.

Depending on the measurement, two types of results can be expected from an experiment. Either an experiment shows a new source of signal events and a discovery can be claimed, or, when the measurement is consistent with the background-only hypothesis, an upper limit can be reported on the assumed signal flux. Both results require a different optimisation, as described for instance in the paper by Hill et al. [2005]. For ANTARES the optimisation will be done to set the best upper limit (i. e. the upper part of a confidence interval), for KM3NeT also the optimisation for a discovery will be used, see section 6.2.1.

MRF: Model Rejection Factor

In order to optimise for the best upper limit, the MRF technique is used. The MRF technique is often used in neutrino astronomy as an unbiased method to optimise the experiment for the best sensitivity [Hill and Rawlins, 2003]. The method yields the cuts that minimise the average expected upper limit, under the assumption there is no true signal present.

Since the actual upper limit is not known before the measurement, the average upper limit can be determined that would be obtained when repeating the experiment a large number of times. This average upper limit is the sum of the upper limits for all possible values of n_{obs} and n_{bg}, weighted with their Poisson probabilities of occuring:

$$\bar{\mu}^{\alpha}(n_{obs}, n_{bg}) = \sum_{n_{obs}=0}^{\infty} \sum_{n_{bg}=0}^{\infty} \mu^{\alpha}(n_{obs}, n_{bg}) \frac{\mu_b^{n_{obs}} e^{-\mu_b}}{n_{obs}!} \frac{(\tau\,\mu_b)^{n_{bg}} e^{-\tau\,\mu_b}}{n_{bg}!}, \tag{5.5}$$

where $\mu^{\alpha}(n_{obs}, n_{bg})$ is the event upper limit at a confidence level of α (i. e. μ_{up} in equation 5.4).

The MRF is then defined as the average upper limit divided by the expected signal:

$$\mathrm{MRF} = \frac{\bar{\mu}^{\alpha}(n_{obs}, n_{bg})}{\mu_s}. \tag{5.6}$$

---

[28] *The interval is in this case also called conservative.*

The MRF shows how much the sensitivity of the experiment is above (or below) the signal flux model (so an MRF of 10 means that the experiment is sensitive to fluxes at least 10 times higher than the assumed signal flux model). By optimising the cuts to get the lowest MRF, the sensitivity of the experiment is maximised.

To determine the event upper limits, the profile likelihood method is used. In this method, the multi-dimensional likelihood function is reduced to a function that only depends on the parameter of prime interest. In the case at hand, the likelihood function is given by:

$$\mathcal{L}(\mu_\mathrm{b}, \mu_\mathrm{s} | n_\mathrm{obs}, n_\mathrm{bg}) = P(n_\mathrm{obs}, n_\mathrm{bg} | \mu_\mathrm{b}, \mu_\mathrm{s}; \tau), \tag{5.7}$$

and the parameter of prime interest is the expected number of signal events (for which the upper limit is determined). The expected number of background events is a so-called nuisance parameter. By fixing μ_s and maximising the likelihood over μ_b alone, the maximum-likelihood estimator of μ_b (denoted by $\hat{\mu}_\mathrm{b}$) is obtained as a function of μ_s:

$$\hat{\mu}_\mathrm{b}(\mu_\mathrm{s}) = \frac{n_\mathrm{obs} + n_\mathrm{bg} - (1+\tau)\mu_\mathrm{s} + \sqrt{[n_\mathrm{obs} + n_\mathrm{bg} - (1+\tau)\mu_\mathrm{s}]^2 + 4(1+\tau)\mu_\mathrm{s}}}{2(1+\tau)}. \tag{5.8}$$

The profile likelihood is then given by:

$$\lambda(\mu_\mathrm{s} | n_\mathrm{obs}, n_\mathrm{bg}) = \frac{\mathcal{L}(\hat{\mu}_\mathrm{b}(\mu_\mathrm{s}), \mu_\mathrm{s} | n_\mathrm{obs}, n_\mathrm{bg})}{\mathcal{L}(\hat{\hat{\mu}}_\mathrm{b}, \hat{\hat{\mu}}_\mathrm{s} | n_\mathrm{obs}, n_\mathrm{bg})}, \tag{5.9}$$

which is only a function of μ_s and where $\hat{\hat{\mu}}_\mathrm{b} = \frac{n_\mathrm{bg}}{\tau}$ and $\hat{\hat{\mu}}_\mathrm{s} = n_\mathrm{obs} - \frac{n_\mathrm{bg}}{\tau}$ are the maximum-likelihood estimators of μ_b and μ_s respectively (maximising the overall likelihood).

The profile likelihood method is widely used in high energy physics and gamma-ray astronomy (where it is popularised by Li and Ma [1983]) and it provides a very good approximation in the parameter space of interest [Cousins et al., 2008]. The profile likelihood method is implemented in ROOT in the TROLKE class. This method is a fully frequentist implementation and uses a likelihood ratio test to determine the signal upper and lower limits. To speed up the calculations, it makes use of the fact that $-2\log\left(\lambda(\mu_\mathrm{s} | n_\mathrm{obs}, n_\mathrm{bg})\right)$ has an approximate χ^2 distribution with 1 degree of freedom [Rolke et al., 2005].

This frequentist approach is compared to a Bayesian method (using the same profile likelihood) with a flat prior in the left plot

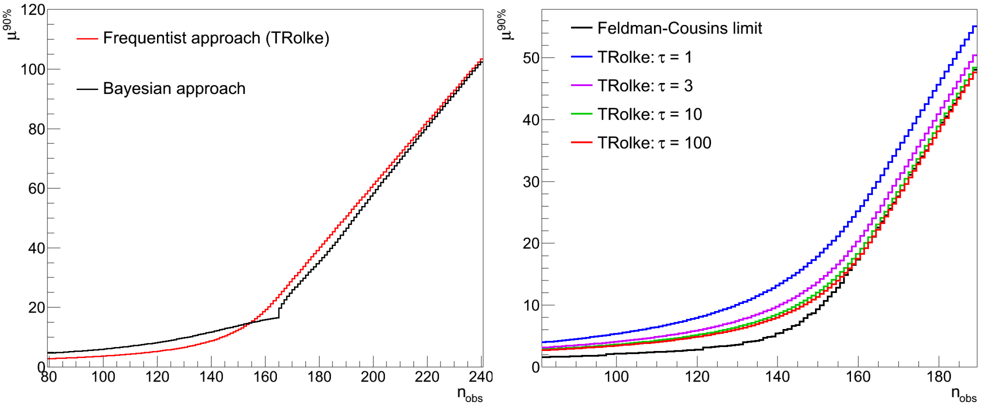

Figure 5.1: 90% CL event upper limit versus number of observed events. LEFT: comparison between frequentist and Bayesian approach for $n_b = 166$ and $\tau = 8$. RIGHT: for $n_b = 166$ for different values of τ.

of figure 5.1 for $\tau = 8$ and $n_b \equiv \frac{n_{bg}}{\tau} = 166$ (which are the number of used background regions and the measured average number of background events per region respectively). The plot shows the 90% confidence level event upper limit as a function of the number of observed events. It can be seen that the obtained event upper limits are different for the two approaches, which can be expected. The differences are not that big however. For this work, the frequentist method as implemented in ROOT is used.

The effect of τ on the event upper limit is shown in the right plot of figure 5.1, for $n_b = 166$ and $\alpha = 90\%$. The higher the value of τ, the better the limit becomes, which is expected since the uncertainty on the background becomes less for increasing values of τ. Also shown is the signal upper limit obtained with the Feldman-Cousins (FC) method, which assumes that the expected number of background events is known exactly [Feldman and Cousins, 1998]. When choosing a high value for τ, for instance 100, so that the uncertainty on the background measurement becomes negligible, it is expected that the limit from the TROLKE method becomes similar to that from the FC method. It can be seen that this is the case when $n_{obs} > n_b$, but not for smaller values of n_{obs}. The upper limit obtained with the TROLKE method is slightly higher for those cases, which is because the method overcovers [Rolke et al., 2005]. This is no problem however, since care must be taken in interpreting the limit anyway in the case that the number of observed events is lower than what is expected from background.

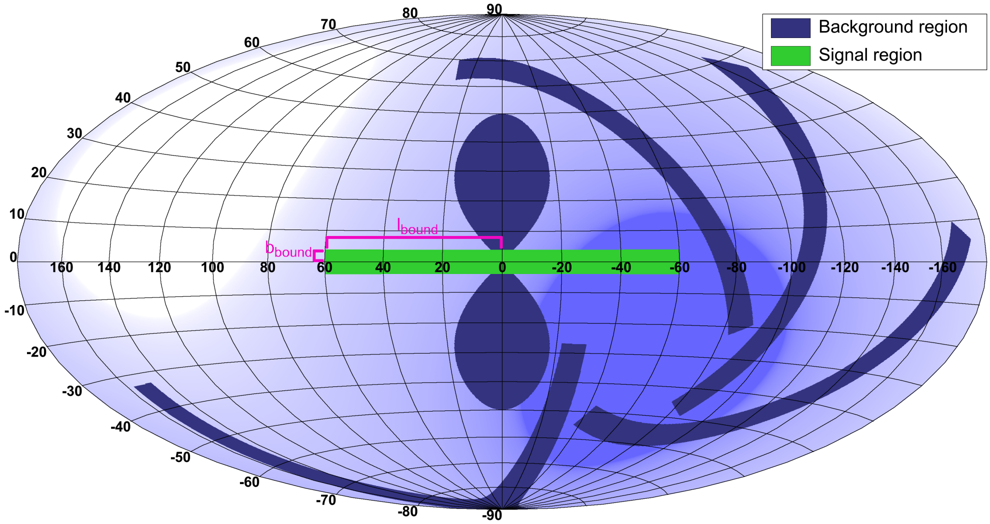

Figure 5.2: Signal and background regions overlaid on the ANTARES visibility for $l_{\text{bound}} = 60^\circ$ and $b_{\text{bound}} = 4^\circ$. Also shown is the signal region used in the Fermi bubble analysis.

5.1.2 *Construction of the background regions*

The analysis method, using an on-source (signal) and an off-source region region, is applied as follows. First, a signal region of a specific size is chosen, which is centred at the Galactic centre. The signal region can be characterised by two parameters, l_{bound} and b_{bound}, which denote the extension in longitude and latitude respectively. For example, a region with $l_{\text{bound}} = 60^\circ$ and $b_{\text{bound}} = 4^\circ$ will extend from a Galactic longitude of -60° to $+60^\circ$ and from a Galactic latitude of -4° to $+4^\circ$, see also figure 5.2 (another example can be found in figure 5.5).

Then, the signal region is converted to local detector coordinates (zenith and azimuth) at an arbitrary time t. The signal region is subsequently converted back to Galactic coordinates at a later time t_1. The time t_1 is thereby chosen such, that the time-shifted region does not overlap with the signal region. Using the fact that a given point in Galactic coordinates follows the same path in detector coordinates every sidereal day, this time-shifted region (background region 1) will follow the exact same path in detector coordinates as the signal region, but with some time offset $\delta t_1 = t_1 - t$. In one sidereal day the expected number of background events is then the same in both regions.

The process is repeated and a second background region is created in the same way, which again follows the same path in detector coordinates, but with a time offset of $\delta t_2 = t_2 - t$ compared to the signal region. This second time offset is chosen such that background region 2 does not overlap with background region 1 to avoid double counting of events. The process is repeated until $t_\mathrm{n} = t + T$, where $T = 23.9345\,\mathrm{day}$ corresponds to one sidereal day. As a result $N = n - 1$ background regions are created. This can be summarised as:

$$\delta t_i = i \cdot T/(N+1), \tag{5.10}$$

which shows the time offset of region i compared to the signal region. The value of N depends on the size of the signal region (compare figures 5.2 and 5.5). Figure 5.3 shows the possible number of background regions for different values of the l_bound and b_bound parameters.

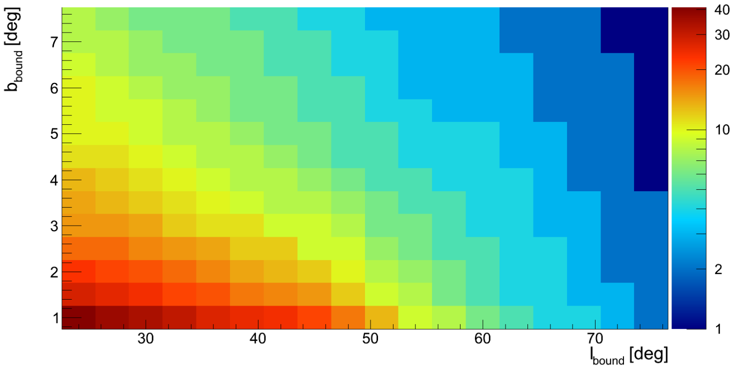

Figure 5.3: Number of background regions as a function of l_bound and b_bound.

In order to do a proper background measurement with the generated background regions, no significant signal must be present in those regions. For this reason, the background regions which overlap with the signal region used in the Fermi bubble analysis are skipped. The regions which partly overlap with the Galactic plane are not skipped, since no significant signal is expected where these regions cross the Galactic plane.

The advantage of defining the background regions in this way is that most systematic effects cancel out. Since the detector response to each of the background regions should be identical by construction, the number of events can be compared to check for any remaining systematic biases. This is presented in section 5.2.

5.1.3 *Signal region optimisation*

In total there are 6 parameters to optimise (2 parameters for the size of the signal region and 4 cut parameters). Since optimising all 6 parameters at the same time is extremely time consuming, the optimisation is split into two parts. First the size of the signal region is optimised for fixed values of the cut parameters and then the values of the 4 cut parameters are optimised. By factorising the problem, it is possible that the obtained combination of parameters is not optimal. This is investigated by checking the stability of the optimal size of the signal region when using different combinations of the quality cuts.

The optimisation of the size of the signal region is performed for different cut combinations using the MRF method. In this, the MRF is always calculated at 90% confidence level. As input, the expected number of signal and background events is required, which are obtained from the run-by-run (RBR) MC (see section 4.1.5), using only events that have a reconstructed direction falling in the signal region. The amount of atmospheric muons is again evaluated using equation 4.57.

β-CUT	Λ-CUT	PURITY
1.0°	−5.1	~94%
1.0°	−5.3	~78%
1.0°	−5.4	~63%
2.0°	−5.0	~92%
2.0°	−5.2	~75%
2.0°	−5.3	~60%

Table 5.1: The different cut combinations considered for the optimisation of the signal region size.

For the optimisation, the longitude bound is varied from 24° to 75° in steps of 3° and the latitude bound from 1° to 7.5° in steps of 0.5°. For each combination of longitude and latitude bound the MRF value is calculated. Since the quality cut optimisation is made after choosing the signal region, different sets of cuts with different values for the purity (equation 4.56) are investigated. Only events which are reconstructed as upgoing (i. e. $\cos\hat{\theta} < 0$) are considered and only cuts on the track quality parameters Λ and β are used to check the effect of the purity. In table 5.1 the various cuts are summarised.

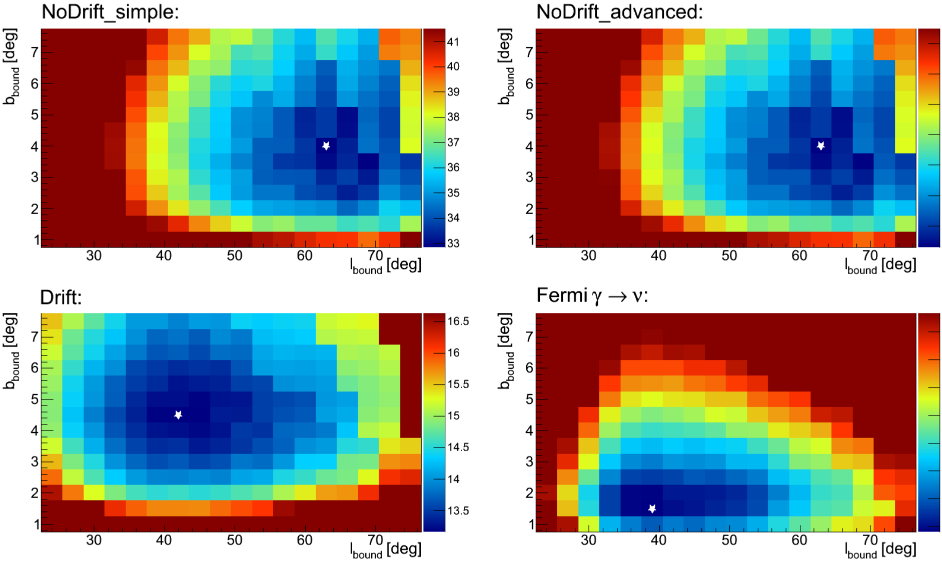

Figure 5.4: MRF versus longitude and latitude bound for an event selection with $\beta < 1.0°$ and $\Lambda > -5.1$. The white star marks the location of the minimum.

Figure 5.4 shows the MRF as a function of longitude bound and latitude bound for an event selection with $\beta < 1.0°$ and $\Lambda > -5.1$ for the four signal flux models. The colour scale shows the value of the MRF and has been chosen such that the blue part of the scale corresponds to the bottom 10% of the MRF values for each signal model. Note that the colour scales are different for each model.

It can be seen that a lower MRF is obtained for the Drift model compared to the NoDrift models, which is expected since the number of signal events is higher in the Drift model. The MRF is also lower for the Fermi $\gamma \rightarrow \nu$ model than for the NoDrift models.

With this particular cut combination, the lowest MRF is found at $l_{\text{bound}} = 63°$ and $b_{\text{bound}} = 4°$ for both NoDrift models, at $l_{\text{bound}} = 42°$ and $b_{\text{bound}} = 4.5°$ for the Drift model and at $l_{\text{bound}} = 39°$ and $b_{\text{bound}} = 1.5°$ for the Fermi $\gamma \rightarrow \nu$ model. It should be noted however that the minimum is quite shallow for each of the models.

The different values of the longitude and latitude bounds obtained for the various signal models are caused by the differences in the predicted angular profile of the flux. By choosing a longitude and latitude bound that is optimal for one model, the sensitivity to the other models is slightly worse. Since the Drift model is more optimistic and the corresponding optimal signal region is in between the optimal regions for the other models, the Drift model will be used for the further optimisation. By choosing this region, the sensitivity to both the NoDrift models and the Fermi $\gamma \rightarrow \nu$ model is about 13% worse than specifically choosing the region that is found optimal for each model.

To check the influence of the uncertainty on the atmospheric neutrino flux, the MRF optimisation is also performed with an increased (25% higher) and decreased (25% lower) atmospheric neutrino flux. The MRF results for the Drift model are summarised in table 5.2. The results for the other models are not shown, since they are not used for the optimisation, but the main conclusions which apply to the Drift model also apply to the other three models.

It can be seen that a looser cut on Λ gives more signal and more background and that for both β cuts the middle Λ cut gives the lowest MRF. This is expected, since cutting too hard on Λ not only removes a lot of misreconstructed atmospheric muons, but also removes a lot of signal. On the other hand, too loose a cut leaves more signal but also more background. The optimal signal region is not very dependent on the purity of the final event sample; for both β cuts the same size of the signal region is found to within a few degrees for the different Λ cuts.

The optimal signal region size has a small dependency on β. When comparing the cut of $\beta < 1.0°$, $\Lambda > -5.1$ with $\beta < 2.0°$, $\Lambda > -5.0$ (which have a comparable purity), it can be seen that the former results in a better MRF value. This is caused by the fact that a harder Λ cut is required in order to get the same purity for a looser β cut. To compensate for the loss in signal, the signal region has to be made bigger which also gives more background. It means that the optimisation of the signal region size and the cuts are correlated: for a more optimal set of cuts (i. e. a set of cuts resulting in a lower sensitivity), a smaller signal region is found to be optimal. The effect is however quite small.

The effect of using a cut on E_{rec} has also been checked, but the optimal size of the signal region does not change [Visser, 2014]. The effect of using the R_{GF} cut has not been checked explicitly, but since it is expected that using it in combination with Λ and β will increase the neutrino efficiency, it is reasonable to assume a slightly smaller optimal size of the signal region will be found

CUT COMBINATION	ATMOSPHERIC ν-FLUX	OPTIMAL VALUES l_{bound}	b_{bound}	MRF	μ_{s}	μ_{b}
$\beta < 1.0°, \Lambda > -5.1$	Default	42°	4.5°	13.17	1.34	78.4
	25% increased	42°	4.5°	14.59	1.34	97.2
	25% decreased	45°	5°	11.56	1.46	70.4
$\beta < 1.0°, \Lambda > -5.3$	Default	39°	4.5°	12.99	1.64	118
	25% increased	39°	4.5°	14.23	1.64	143
	25% decreased	39°	4.5°	11.63	1.64	93.5
$\beta < 1.0°, \Lambda > -5.4$	Default	39°	4.5°	13.89	1.81	167
	25% increased	39°	4.5°	15.02	1.81	195
	25% decreased	39°	4.5°	12.69	1.81	138
$\beta < 2.0°, \Lambda > -5.0$	Default	45°	5°	14.03	1.30	82.1
	25% increased	45°	5°	15.48	1.30	101
	25% decreased	51°	5°	12.39	1.38	71.1
$\beta < 2.0°, \Lambda > -5.2$	Default	45°	5°	13.88	1.57	122
	25% increased	51°	5°	15.13	1.87	201
	25% decreased	51°	5°	12.55	1.87	137
$\beta < 2.0°, \Lambda > -5.3$	Default	51°	5°	14.76	2.12	247
	25% increased	48°	4°	15.77	1.84	217
	25% decreased	48°	4°	13.62	1.84	160

Table 5.2: Optimal longitude and latitude bounds and obtained MRF value for the Drift model for the considered cuts.

when used. Again, the effect is expected to be small[29].

The effect of an increased/decreased atmospheric neutrino background is only an increase/decrease in the MRF; (almost) the same size of the signal region is found to be optimal when varying the atmospheric neutrino flux. For an increased background a slightly smaller region seems optimal for some cut combinations, but the effect is negligible.

From the information in the table it can be concluded that a region with $l_{\text{bound}} = 39°$ and $b_{\text{bound}} = 4.5°$ is optimal. The signal region has a size of 0.21 sr, and 8 background regions can be used. The signal and background regions are shown in figure 5.5.

[29] *The signal region optimisation has been repeated with the optimal cuts (equation 5.19) to check this explicitly, resulting in the same optimal size of* $l_{bound} = 39°$ *and* $b_{bound} = 4.5°$.

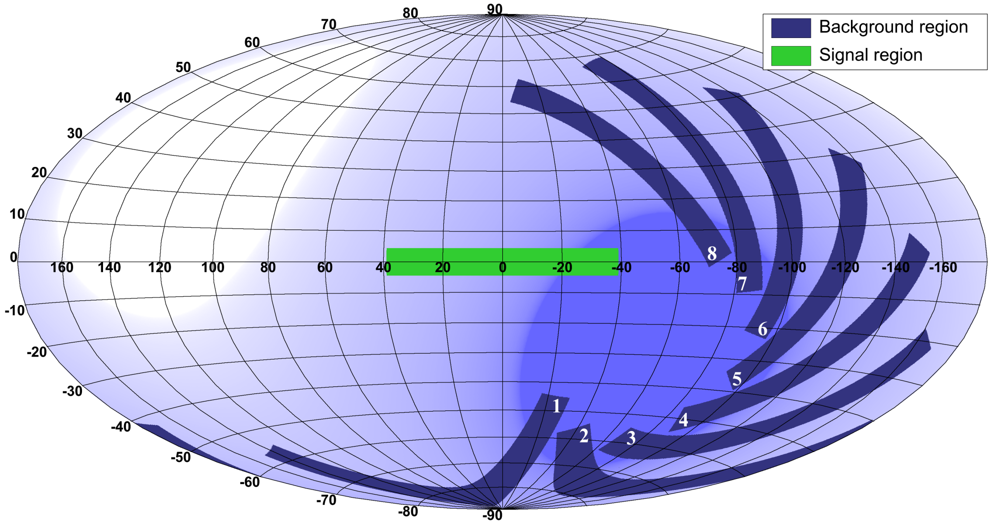

Figure 5.5: Signal and background regions for the optimised signal region ($l_{\text{bound}} = 39^\circ$ and $b_{\text{bound}} = 4.5^\circ$) overlaid on the ANTARES visibility. The numbering of the background regions is also shown.

5.2 CHECKS ON THE BACKGROUND REGIONS

Now that the optimal signal region has been determined and the background regions defined, some checks can be performed on the background regions. It can be seen from figure 5.5 that each background region has the same visibility. However, systematic biases can arise, because data taking is not continuous. There is for instance a small amount of time between two data runs in which no data are taken, and also no physics data are taken during calibration of the detector. In addition, not all physics data runs are suitable for analyses (see section 5.2.1). The gaps in data taking can result in some regions having a higher/lower visibility than others, so that the background regions are no longer identical.

In order to check for this possibility, the effective visibility is calculated and presented in section 5.2.2 and a check for any systematic bias is made and presented in section 5.2.3.

Finally, a comparison between the data and the MC simulation is made and presented in section 5.2.4. A good agreement between data and MC is required, since the MC is used to optimise the quality cuts and to convert the measured number of events into a flux limit.

5.2.1 *Data selection*

For this analysis, the data from January 29th 2007 (run 25682) to November 30th 2012 (run 68170) are used. In this period, a total of 15982 data runs are taken, in which either the 3N, the 2T3 or the TQ trigger were active (or a combination of them). From these data runs, only those runs are used that are suitable for data analysis. For this, the run duration has to be more than one second and there should not be any serious problems. In addition, all SCAN runs and all SPARKING runs are excluded. SCAN runs are runs which are used to test new calibrations or detector settings. SPARKING runs contain events which are caused by a sparking PMT. Finally, the reconstruction algorithms (AAFIT, GRIDFIT) should have been applied to the data and there should be matching run-by-run MC files.

SELECTION STEP	NUMBER OF DATA RUNS THAT PASS
Total number of physics data runs	15982
+ Suitable for data analysis	15172
+ Is not a SCAN run	13529
+ Is not a SPARKING run	13481
+ Reconstruction applied	13223
+ RBR MC files exist	12377

Table 5.3: The number of data runs selected after applying selection criterea.

After these selection criteria, a total of 12377 runs are selected, which have a combined total livetime of 1288 days (3.53 years). Table 5.3 lists the number of data runs selected by applying the selection criterea. From the selected runs, all events that are either triggered by the 3N, the 2T3 or the TQ trigger are used.

5.2.2 *Effective visibility*

The visibility of ANTARES is shown in figure 2.29 (and in figure 5.5). It is calculated by taking a given direction in Galactic coordinates and checking for which fraction of a sidereal day it is visible (i. e. has a zenith angle above 90°). This is the theoretical visibility, in that it would be obtained if the ANTARES detector would measure continuously for a sidereal day, or any integer multiple of it. In reality however, the data taking is not continuous, so there are parts of a sidereal day for which no data are taken. This affects the visibility and can lead to systematic biases. This can best be illustrated by an example.

Consider a total livetime of exactly 10 sidereal days and a specific direction (in the signal region) which is visible during 80% of a sidereal day. If data taking is continuous over the whole livetime, the visibility of this direction is just $\mathcal{V} = 80\%$ (equation 2.63). Now consider that a calibration run of 2 hours is taken on one of the days, during a time in which the direction can be observed (i. e. it is visible). For the sidereal day in which this calibration run is done, the direction is only seen during 78.2% of the time when physics data are taken (so excluding the calibration run). The effective visibility of the direction is averaged over the whole livetime and is defined as:

$$\mathcal{V}_{\text{eff}} = \frac{\int_{T_{\text{start}}}^{T_{\text{stop}}} \mathrm{d}t\, v(l, b, t) A(t)}{\int_{T_{\text{start}}}^{T_{\text{stop}}} \mathrm{d}t\, A(t)}, \tag{5.11}$$

where $v(l, b, t)$ is as defined in equation 2.64, T_{start} and T_{stop} are the time when data taking starts and stops respectively and with:

$$A(t) = \begin{cases} 1 & \text{If 'good' physics data are taken} \\ 0 & \text{Otherwise} \end{cases} \tag{5.12}$$

Using equation 5.11 gives $\mathcal{V}_{\text{eff}} = 79.8\%$ in the example above. Note that the effective visibility is defined such that it is unaffected if the calibration run would last exactly one sidereal day.

Consider now a second direction (e. g. from one of the background regions), that should by construction have the same visibility as the direction considered above (80%). However, during the time the calibration run is performed, this direction is above the horizon and so is not visible, giving $\mathcal{V}_{\text{eff}} = 80.7\%$. The fact that the effective visibilities are different for both directions results in a systematic bias. The same number of events is expected from each of the directions within the statistical uncertainty, but a different number of events is actually measured.

Using again the fact that a given direction in Galactic coordinates has the same local detector coordinates after one sidereal day has passed, the effective visibility can be rewritten as:

$$\mathcal{V}_{\text{eff}} = \int_0^T \mathrm{d}t\, w(t)\, v(l, b, t), \tag{5.13}$$

where $w(t)$ is the sidereal day weight, which represents in which fraction of the livetime data are taken at that time of the sidereal day. In case of continuous data taking, $w(t)$ would have a value of $1/T$ and the effective visibility (equation 5.13) would be identical to the theoretical visibility (equation 2.63). If, on the other hand, only during the first 3 hours of the sidereal day data would be taken, the value of $w(t)$ would be $1/(3\,\text{hour})$ for the first 3 hours and 0 for the rest of the day. By dividing the sidereal day in 1657 bins of 52 s each, the integral in equation 5.13 becomes a sum, and the value of $w(t)$ would be $1/1657$ for each bin in case of continuous data taking.

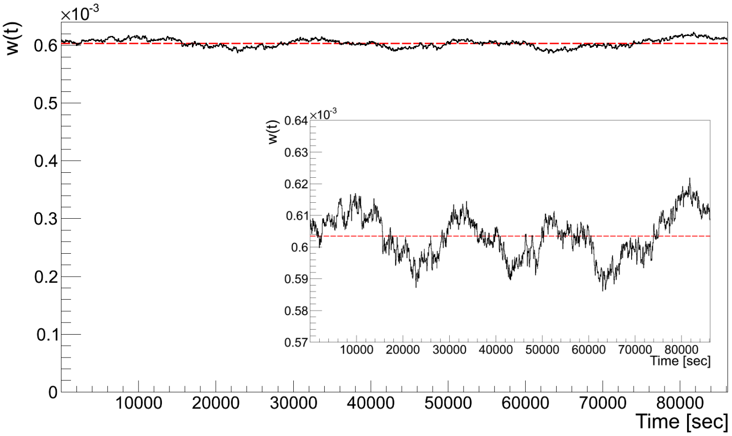

Figure 5.6: Sidereal day weight $w(t)$ versus time for the 12377 selected data runs. The red line indicates the theoretical value assuming there is continuous data taking. The same results are shown in the inset, but focused around the average weight.

The distribution of $w(t)$ for the 12377 data runs that are selected is shown in figure 5.6. For each data run that is selected, the start and stop times are taken and converted to sidereal time. The bins corresponding to the time period between start and stop times are filled with a value of 1. The histogram is then normalised. The red dashed line shows the fraction obtained when data taking would be continuous over the whole sidereal day.

From the inset in the figure, the effect of the data run selection can be more appreciated. The discontinuity of the data taking results in a higher fraction of the data runs being taken during certain parts of a sidereal day than for others. The differences compared to the red line are about 3%.

Since different parts of the sidereal day get a different weight, the effective visibility is expected to look different from the theoretical visibility. By eye however, the effective visibility looks

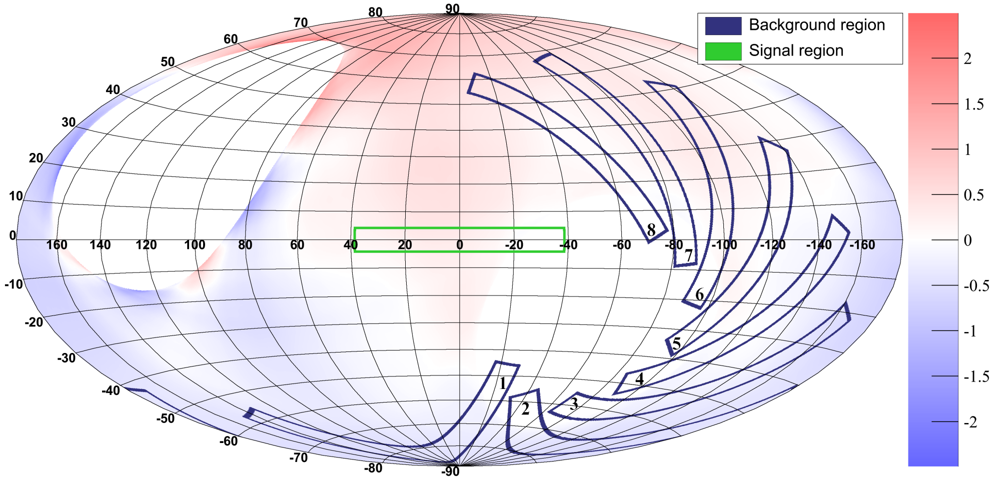

Figure 5.7: The percentual differences between the effective and the theoretical visibility.

the same as the theoretical visibility. The small differences can be visualised by calculating the percentual differences between the effective and the theoretical visibility:

$$\Delta\mathcal{V} = \frac{\mathcal{V}_{\text{eff}} - \mathcal{V}}{\mathcal{V}} \cdot 100\%. \tag{5.14}$$

The sky-map of $\Delta\mathcal{V}$ is shown in figure 5.7.

From the figure it can be seen that the visibility is unchanged in the two parts of the sky that are either never or always visible, as is expected. For the other directions there are some small differences; for most of the directions the difference is around 5‰. The maximum differences are found near the region which is never visible and are about 2.5%. Since the visibility of these directions is low, the impact of these differences is small.

The borders of the signal and background regions are also shown in the figure. It can be seen that part of regions 1, 2, 3 and to a lesser extent 4, lies in the blue part, so slightly less events are expected in those regions. Part of regions 6, 7 and 8, as well as part of the signal region, lies in the red part and slightly more events are expected in those regions. Region 5 lies mostly in the white part, so is unchanged as to the expectation from the theoretical visibility. However, since only a part of the regions lies in the blue/red part, and the differences in the regions are less than a percent, no significant differences are expected between the regions.

5.2.3 *Checking for systematic biases*

On the basis of the effective visibility, it is found that the same number of events is expected in the signal and background regions to within one percent. To check for remaining systematic biases, the number of data events in each of the 8 background regions is counted and compared to each other. In order to reject badly reconstructed events and keep sufficient statistics, only upgoing events with $\Lambda > -6.0$ and $\beta < 1.75^\circ$ are considered. Table 5.4 shows the number of events surviving this cut for each of the 8 regions; for the numbering of the regions see figure 5.5.

BACKGROUND REGION	NUMBER OF EVENTS	BACKGROUND REGION	NUMBER OF EVENTS
1	8920 ± 94	5	9000 ± 95
2	8945 ± 95	6	8881 ± 94
3	9022 ± 95	7	8934 ± 95
4	8983 ± 95	8	8826 ± 94

Table 5.4: Number of events reconstructed as upgoing (with $\Lambda > -6.0$ and $\beta < 1.75^\circ$) in each of the 8 background regions. The error on the number of events is the statistical uncertainty.

The numbers of events obtained from the 8 regions are consistent within the statistical uncertainties. It can thus be concluded that there are no big systematic biases. To carry out a more thorough check, the number of events surviving in each region is subdivided into multiple 'measurements', by defining several cut regions.

In order to make these comparisons, a certain cut combination is applied and the surviving events are counted, giving n_i events for region i. This number of events is then compared to the average number of events from the other 7 regions, n_{av}, giving an event-ratio:

$$R_i = \frac{n_i}{n_{\mathrm{av}}}, \tag{5.15}$$

with an error of:

$$\delta R_i = R_i \cdot \sqrt{\left(\frac{\delta n_i}{n_i}\right)^2 + \left(\frac{\delta n_{\mathrm{av}}}{n_{\mathrm{av}}}\right)^2}, \tag{5.16}$$

where δn_i and δn_{av} are the statistical uncertainties on n_i and n_{av} respectively.

NUMBER	CUT COMBINATION	NUMBER	CUT COMBINATION
1	$\beta \leqslant 1.0°$, $-6 \leqslant \Lambda < -5.99$	19	$\beta \leqslant 1.0°$, $-5.59 \leqslant \Lambda < -5.45$
2	$\beta \leqslant 1.0°$, $-5.99 \leqslant \Lambda < -5.98$	20	$\beta \leqslant 1.0°$, $\Lambda \geqslant -5.45$
3	$\beta \leqslant 1.0°$, $-5.98 \leqslant \Lambda < -5.97$	21	$1.0° < \beta \leqslant 1.05°$, $\Lambda \geqslant -6.0$
4	$\beta \leqslant 1.0°$, $-5.97 \leqslant \Lambda < -5.96$	22	$1.05° < \beta \leqslant 1.1°$, $\Lambda \geqslant -6.0$
5	$\beta \leqslant 1.0°$, $-5.96 \leqslant \Lambda < -5.95$	23	$1.1° < \beta \leqslant 1.15°$, $\Lambda \geqslant -6.0$
6	$\beta \leqslant 1.0°$, $-5.95 \leqslant \Lambda < -5.93$	24	$1.15° < \beta \leqslant 1.2°$, $\Lambda \geqslant -6.0$
7	$\beta \leqslant 1.0°$, $-5.93 \leqslant \Lambda < -5.92$	25	$1.2° < \beta \leqslant 1.25°$, $\Lambda \geqslant -6.0$
8	$\beta \leqslant 1.0°$, $-5.92 \leqslant \Lambda < -5.91$	26	$1.25° < \beta \leqslant 1.3°$, $\Lambda \geqslant -6.0$
9	$\beta \leqslant 1.0°$, $-5.91 \leqslant \Lambda < -5.89$	27	$1.3° < \beta \leqslant 1.35°$, $\Lambda \geqslant -6.0$
10	$\beta \leqslant 1.0°$, $-5.89 \leqslant \Lambda < -5.87$	28	$1.35° < \beta \leqslant 1.4°$, $\Lambda \geqslant -6.0$
11	$\beta \leqslant 1.0°$, $-5.87 \leqslant \Lambda < -5.85$	29	$1.4° < \beta \leqslant 1.45°$, $\Lambda \geqslant -6.0$
12	$\beta \leqslant 1.0°$, $-5.85 \leqslant \Lambda < -5.83$	30	$1.45° < \beta \leqslant 1.5°$, $\Lambda \geqslant -6.0$
13	$\beta \leqslant 1.0°$, $-5.83 \leqslant \Lambda < -5.81$	31	$1.5° < \beta \leqslant 1.55°$, $\Lambda \geqslant -6.0$
14	$\beta \leqslant 1.0°$, $-5.81 \leqslant \Lambda < -5.78$	32	$1.55° < \beta \leqslant 1.6°$, $\Lambda \geqslant -6.0$
15	$\beta \leqslant 1.0°$, $-5.78 \leqslant \Lambda < -5.75$	33	$1.6° < \beta \leqslant 1.65°$, $\Lambda \geqslant -6.0$
16	$\beta \leqslant 1.0°$, $-5.75 \leqslant \Lambda < -5.71$	34	$1.65° < \beta \leqslant 1.7°$, $\Lambda \geqslant -6.0$
17	$\beta \leqslant 1.0°$, $-5.71 \leqslant \Lambda < -5.66$	35	$1.7° < \beta \leqslant 1.75°$, $\Lambda \geqslant -6.0$
18	$\beta \leqslant 1.0°$, $-5.66 \leqslant \Lambda < -5.59$		

Table 5.5: The 35 cut regions that are used for determining the event-ratios from the ANTARES data.

If no systematic bias is present, the distribution of the calculated event-ratios will be a Gaussian centred at 1 with a width corresponding to the total number of events. In case a systematic bias is present, the mean of the Gaussian will be offset from 1. The method has been tested by giving one of the regions a systematic bias of $\pm x\%$ which is then noticed as a shift in the central value equal to the same percentage [Visser, 2014].

For the application to data, a total of 35 measurements are defined, which are summarised in table 5.5. The cuts are chosen such, that the total number of events is more or less evenly distributed over the measurements. It should be noted that except for the $\beta \leqslant 1.0°$, $\Lambda \geqslant -5.45$ cut (which has a purity of about $60 \pm 1\%$), the measurements are dominated by atmospheric muons.

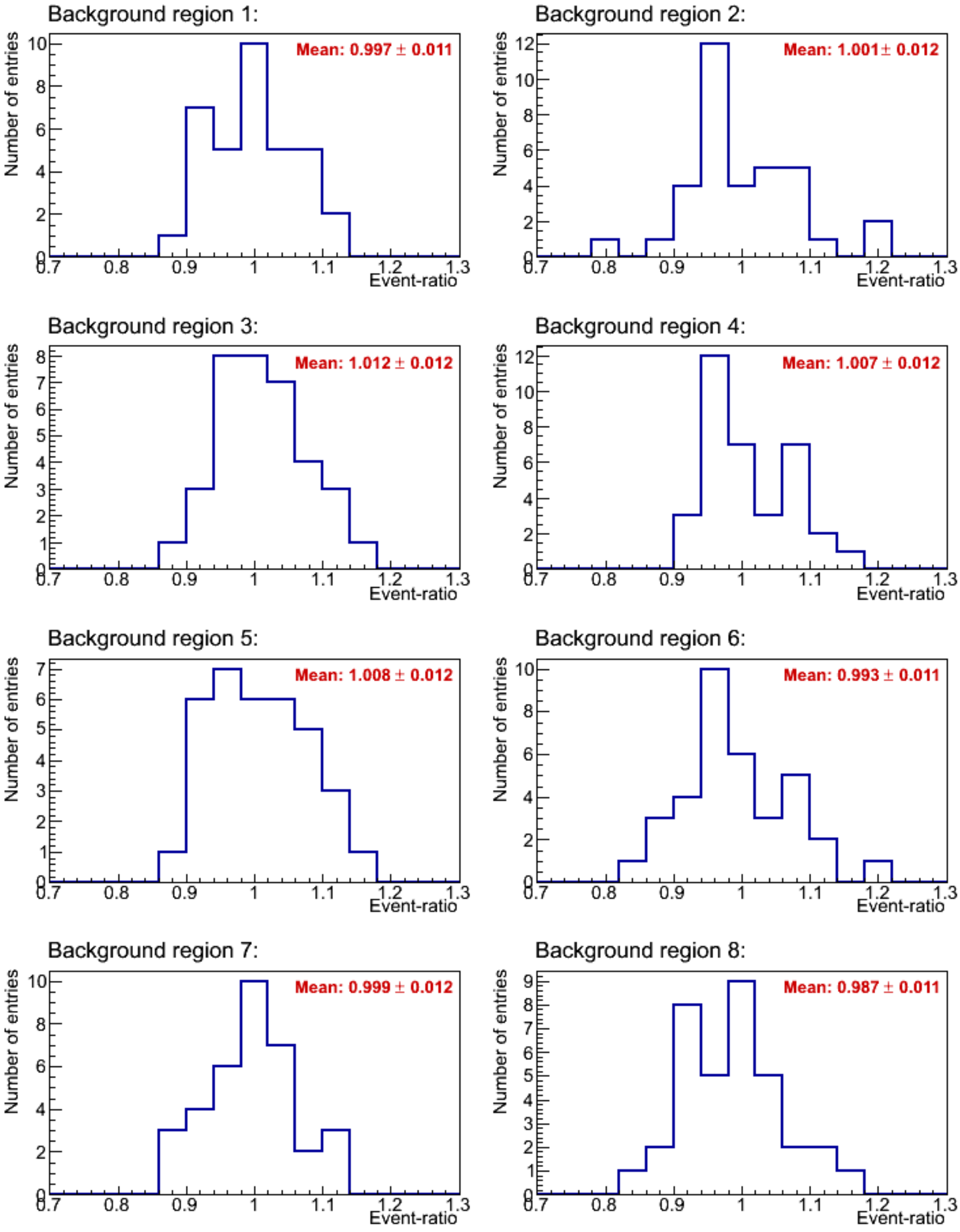

Figure 5.8: Event-ratio distributions for the ANTARES data for the different background regions.

The event-ratio distributions for the ANTARES data are shown in figure 5.8 for the different background regions. The mean of the distribution (i. e. the average event-ratio for that background region) is shown in red in the plot. The error on the mean is also shown, which has been calculated from the error on the event-ratio (equation 5.16) using error propagation. It can be seen that the mean of the event-ratio distribution for each background region is compatible with 1 within the uncertainty. The remaining systematic biases are then limited to about 1%.

5.2.4 *Data-MC comparison*

Finally, the agreement between data and the run-by-run MC simulation is checked for all events that are reconstructed in the background regions. Data-MC comparison plots are made for the 6 key parameters, which are the reconstructed zenith and azimuth angles ($\hat{\theta}$ and $\hat{\phi}$ respectively) and the four cut parameters: Λ, β, E_{rec} and R_{GF}.

For the plots, the following cuts are applied:

- $\cos\hat{\theta} < 0$
- $\Lambda > -5.8$
- $\beta < 10.0^\circ$
- $\log_{10}(E_{\text{rec}}) > 2.0$
- $R_{\text{GF}} > 1.35$ (5.17)

which corresponds to the loosest combination of cuts considered in the optimisation (see section 5.3.3).

The plots are shown in figure 5.9. In the plots, the data (in black) are compared to the atmospheric muon simulation (in red) and the atmospheric CC muon-(anti-)neutrino simulation (in purple). For each of the plots all cuts shown in equation 5.17 are applied, except the cut on the variable that is plotted (if applicable). The cut is represented by the dashed dark blue line. In addition, the ratio of data to the sum of both MC contributions is calculated and shown below the corresponding figure; the red line in this plot denotes a ratio of 1.

The agreement between data and MC is reasonable for all variables, but a few remarks must be made. As also found in other analyses, the data exceeds the atmospheric neutrino flux prediction, which can be seen most clearly in the Λ distribution (for $\Lambda > -5$, where the atmospheric muon contribution is small). This is important for the optimisation of the cuts, since a higher

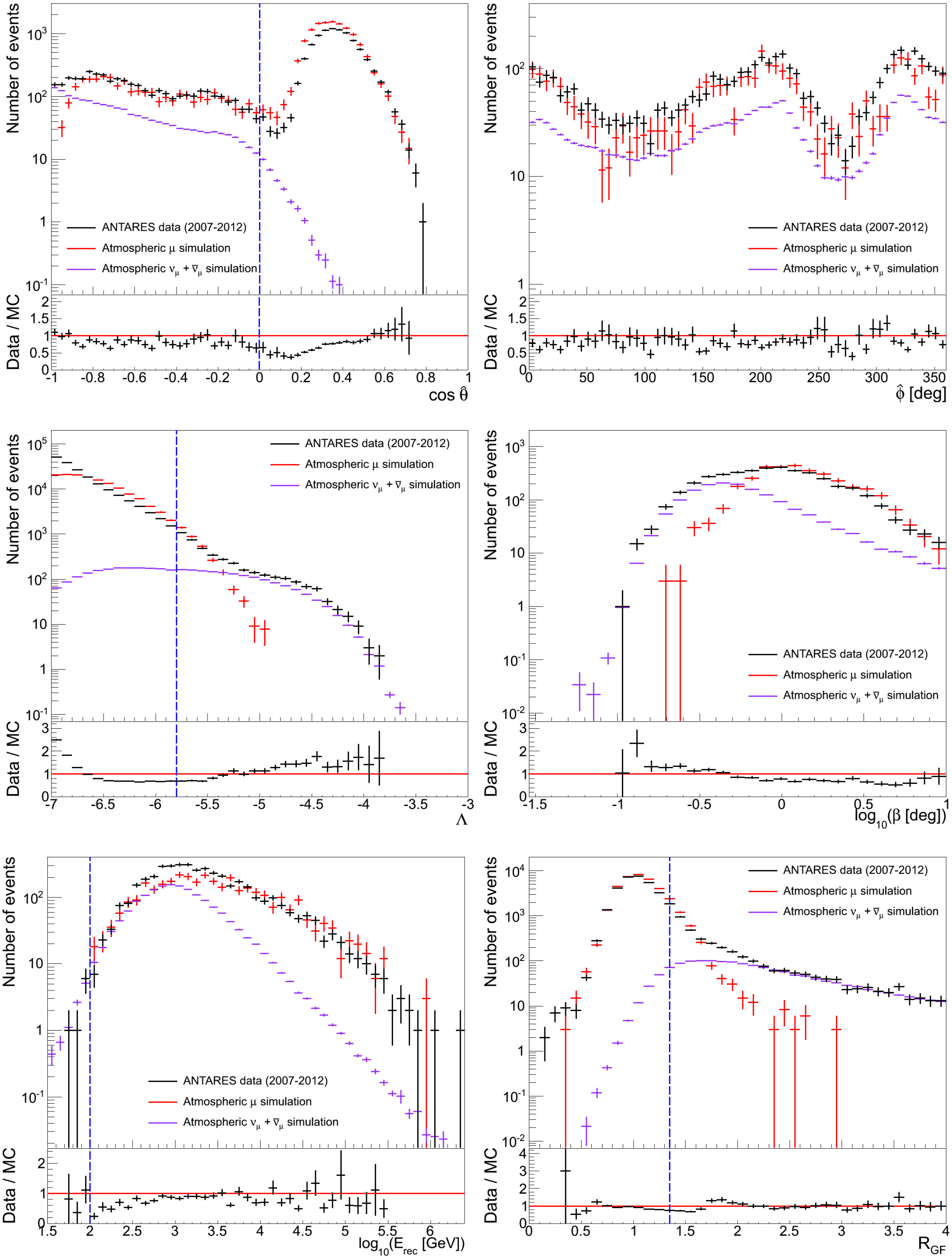

Figure 5.9: Data-MC comparison plots for events from the background regions. TOP LEFT: $\cos\hat{\theta}$ distribution. TOP RIGHT: reconstructed azimuth angle distribution. MIDDLE LEFT: Λ distribution. MIDDLE RIGHT: β distribution. BOTTOM LEFT: $\log_{10}(E_{\text{rec}})$ distribution. BOTTOM RIGHT: R_{GF} distribution.

atmospheric neutrino background might affect the optimal cut values. Instead of an ad hoc scaling of the MC to match the data, the optimisation is repeated for an increased and decreased atmospheric neutrino background. In this way, the influence of the normalisation of the atmospheric neutrino flux can be quantified.

Furthermore, there are some apparent features in the Λ and $\cos\hat{\theta}$ distributions. In the former, the shape of the muon MC is different than the data for low values, while for the latter the shapes are different for downgoing events. These differences are thought to be caused by high optical background [Bogazzi, 2014]. Since the applied cuts avoid these features and the shape of the data is reasonably well described for the regions of interest, this should not be a problem for this analysis.

5.3 EVENT SELECTION

After optimising the size of the signal region and checking for systematic biases, the last step is the optimisation of the cut parameters: Λ, β, E_{rec} and R_{GF}. Since the optimisation problem is 4 dimensional, the process is split into three steps. First the cut on R_{GF} is not applied and the optimal combination of the other three parameters is found; then the same is done for β. This gives an idea about where to look in the cut space, so that the full 4D optimisation can be performed more efficiently.

In the following sections, all events triggered either by the 3N, the 2T3 or the TQ trigger are used and the same cuts are applied regardless of the trigger algorithm. In addition, only events that are reconstructed as upgoing are used. The effect of variable cuts is checked in section 5.3.4. In the following sections, the cut on $\log_{10}(E_{\text{rec}})$ is varied between 2.0 and 3.0 in steps of 0.05. The ranges and step sizes used for Λ, β and R_{GF} vary and are given below.

5.3.1 *Optimisation without R_{GF}*

The MRF is calculated in the same way as for the optimisation of the size of the signal region. The quality cuts are applied, the number of signal and background events is obtained from the run-by-run MC and the MRF is calculated using formula 5.6.

To visualise the 3D cut space, a 2D grid of the MRF versus the applied Λ and $\log_{10}(E_{\text{rec}})$ cuts is made for a fixed value of β, and the minimum is obtained. Examples can be found in figure 5.10.

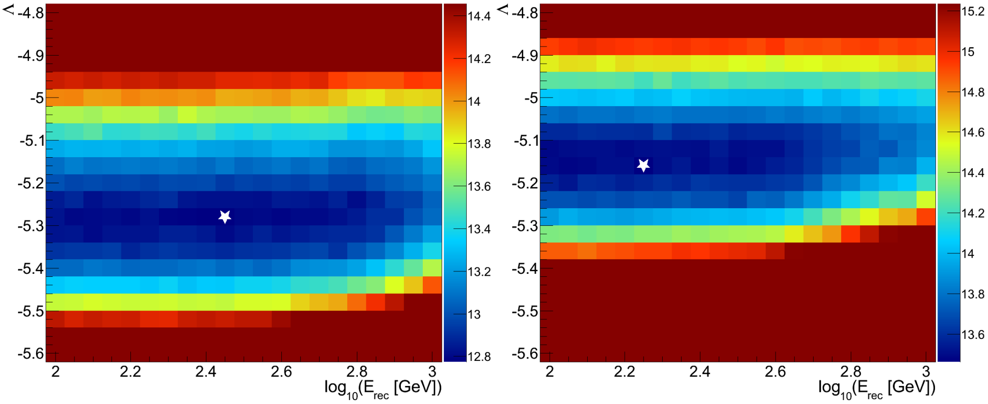

Figure 5.10: MRF versus Λ and $\log_{10}(E_{\mathrm{rec}})$; no R_{GF} cut is applied. The white star marks the location of the minimum. LEFT: for $\beta < 0.7°$. RIGHT: for $\beta < 1.4°$.

This process is repeated for other β values to find the global minimum. The cut on Λ is varied between -5.6 and -4.8 in steps of 0.04 and the cut on β between 0.4° and 1.5° in steps of 0.1°.

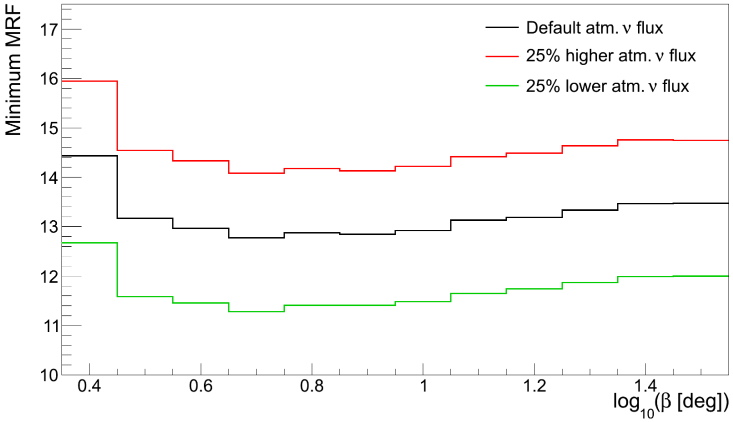

Figure 5.11: Minimum MRF versus β without applying a R_{GF} cut. For each β cut, the Λ and $\log_{10}(E_{\mathrm{rec}})$ cuts have been optimised.

The results of the optimisation are shown in table 5.6 and the minimum MRF is plotted versus β in figure 5.11. It can be seen that the optimal β cut is found at 0.7°, although the minimum is quite shallow. The same β cut is found to be optimal for the increased/decreased atmospheric neutrino flux. Also the energy cut is found to be stable under variation of the atmospheric neutrino flux. The Λ cut does vary however; a looser cut is

ATM. ν FLUX	OPTIMAL CUT VALUES Λ	β	$\log_{10}(E_{\mathrm{rec}})$	MIN. MRF	μ_{s}	μ_{b}	PURITY
Default	-5.28	0.7°	2.45 (= 282 GeV)	12.77	1.47	90.7	92.1%
25% incr.	-5.32	0.7°	2.5 (= 316 GeV)	14.09	1.52	119	91.3%
25% decr.	-5.24	0.7°	2.45 (= 282 GeV)	11.28	1.41	64.3	90.0%

Table 5.6: Optimal cuts and obtained MRF value for the optimisation without R_{GF}.

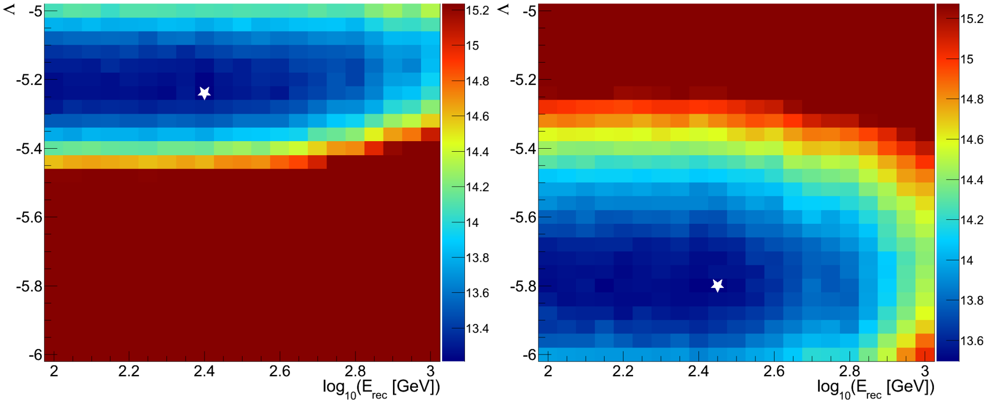

Figure 5.12: MRF versus Λ and $\log_{10}(E_{\mathrm{rec}})$; no β cut is applied. The white star marks the location of the minimum. LEFT: for $R_{\mathrm{GF}} > 1.2$. RIGHT: for $R_{\mathrm{GF}} > 1.8$.

optimal when the atmospheric neutrino background is higher and vice versa. In general, a purity of the final event sample of around 90% is optimal. For a higher atmospheric neutrino flux, more misreconstructed atmospheric muons are allowed in the sample, leading to a looser cut on Λ.

5.3.2 *Optimisation without β*

The same procedure is now applied to determine the optimal cut values without application of the β cut. For this, the cut on Λ is varied between -6.0 and -5.0 in steps of 0.04 and the cut on R_{GF} between 1.0 and 2.0 in steps of 0.1. The Λ-$\log_{10}(E_{\mathrm{rec}})$ grids for two R_{GF} cuts are shown in figure 5.12. It can be seen that the stricter the cut on the R_{GF} parameter is, the looser the Λ cut can be.

The results for the optimisation are shown in table 5.7 and the minimum MRF is plotted versus R_{GF} in figure 5.13. A R_{GF} cut

ATM. ν FLUX	OPTIMAL CUT VALUES Λ	R_{GF}	$\log_{10}(E_{\mathrm{rec}})$	MIN. MRF	μ_{s}	μ_{b}	PURITY
Default	-5.6	1.6	2.55 (= 355 GeV)	12.65	1.79	134	90.1%
25% incr.	-5.64	1.6	2.55 (= 355 GeV)	13.93	1.84	174	90.3%
25% decr.	-5.52	1.6	2.55 (= 355 GeV)	11.18	1.68	90.8	91.1%

Table 5.7: Optimal cuts and obtained MRF value for the optimisation without β.

of 1.6 is found to be optimal, with a Λ cut of -5.6. This value corresponds to a much looser cut compared to when using a cut on β instead of a cut on R_{GF}. It can thus be concluded that the R_{GF} variable is more powerful than β to reject misreconstructed atmospheric muons.

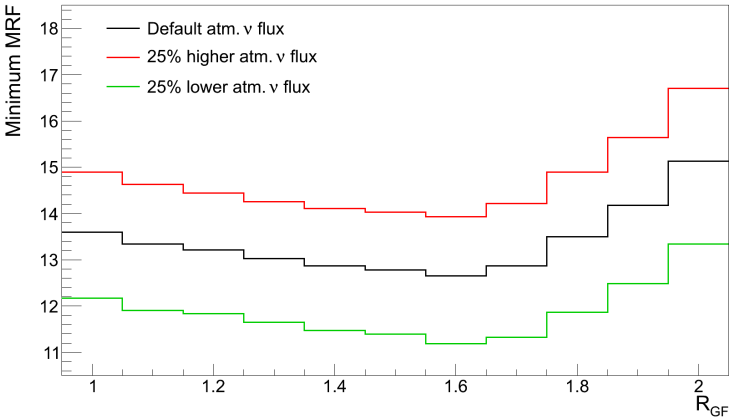

Figure 5.13: Minimum MRF versus R_{GF} without applying a β cut. For each R_{GF} cut, the Λ and $\log_{10}(E_{\mathrm{rec}})$ cuts have been optimised.

An increase or decrease of the atmospheric neutrino background yields the same conclusions as before. The R_{GF} and reconstructed energy cuts are not affected, and a looser Λ cut is found to be optimal for an increased atmospheric neutrino background.

5.3.3 *Full optimisation*

After performing the 3D optimisations, the full 4D optimisation is performed. Using the results from the previous sections, the cut parameters are varied as follows. The cut on Λ is varied between

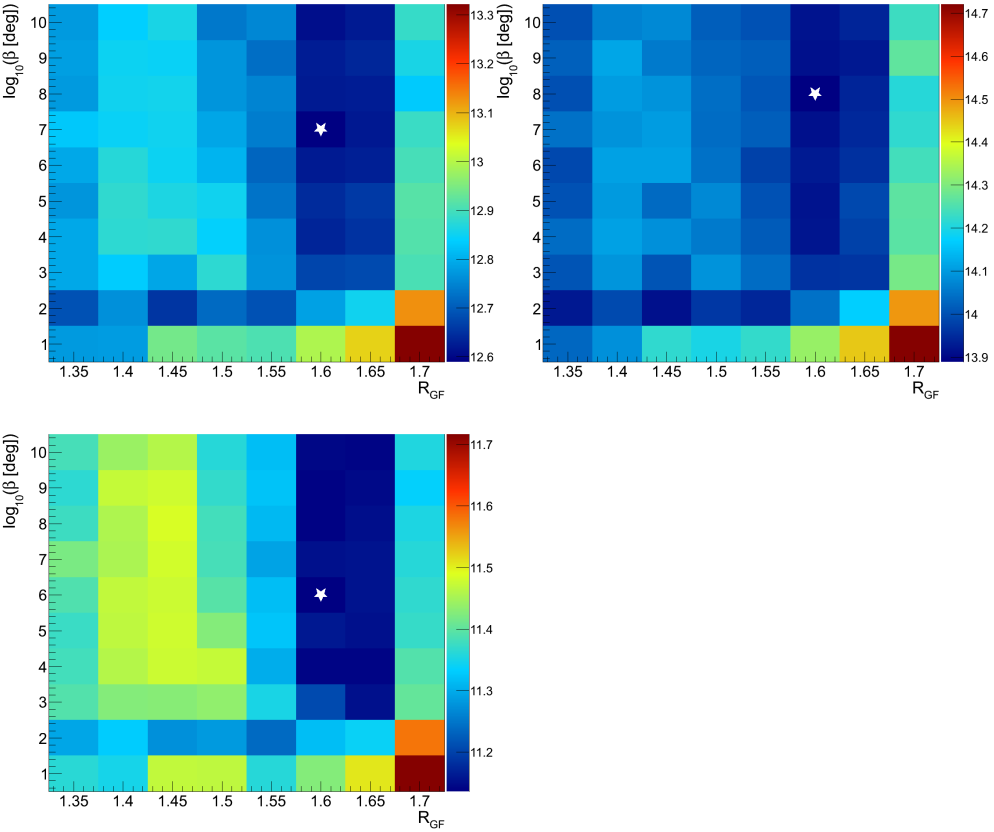

Figure 5.14: Minimum MRF versus R_{GF} and β. For each R_{GF}-β cut combination, the Λ and $\log_{10}(E_{\mathrm{rec}})$ cuts have been optimised. The white star marks the location of the minimum. TOP LEFT: for the default atmospheric neutrino background. TOP RIGHT: for a 25% higher atmospheric neutrino background. BOTTOM LEFT: for a 25% lower atmospheric neutrino background.

-5.8 and -5.2 in steps of 0.04, the cut on R_{GF} between 1.35 and 1.7 in steps of 0.05 and the cut on β between 1.0° and 10.0° in steps of 1.0°.

Like before, the minimum MRF is obtained for fixed R_{GF} and β cuts by finding the minimum in the Λ-$\log_{10}(E_{\mathrm{rec}})$ grid. The results are summarised in table 5.8 and the minimum MRF is plotted versus β and R_{GF} in figure 5.14 for the default atmospheric neutrino flux as well as for the increased/decreased flux.

The same R_{GF} and Λ cut values which were found to be optimal in the previous section are also found to be optimal now, but using the β cut in addition is beneficial, since a slightly lower MRF value is found. The required β cut is quite loose, which

ATM. ν	OPTIMAL CUT VALUES				MIN.			
FLUX	Λ	R_{GF}	β	$\log_{10}(E_{\mathrm{rec}})$	MRF	μ_{s}	μ_{b}	PURITY
Default	−5.6	1.6	7.0°	2.55 (= 355 GeV)	12.59	1.77	131	91.1%
25% incr.	−5.64	1.6	8.0°	2.55 (= 355 GeV)	13.89	1.83	171	91.1%
25% decr.	−5.52	1.6	6.0°	2.55 (= 355 GeV)	11.14	1.67	88.7	92.1%

Table 5.8: Optimal cuts and obtained MRF value for the full optimisation.

can be expected since both Λ and R_{GF} are powerful in removing misreconstructed muons. The results for the increased and decreased atmospheric neutrino background are almost identical to the result for the default atmospheric neutrino flux. As found before, a slightly looser (stricter) cut on Λ is better for a higher (lower) neutrino background. The same holds true for the cut on β, a looser cut on this parameter is better for a higher neutrino background and vice versa.

Since the number of atmospheric neutrinos seems to be higher in data than predicted from the MC (see section 5.2.4), the cut combination corresponding to the increased atmospheric neutrino flux is chosen. The optimal cut combination obtained is then:

- $\cos\hat{\theta} < 0$
- $\Lambda > -5.64$
- $\beta < 8.0°$
- $\log_{10}(E_{\mathrm{rec}}) > 2.55$
- $R_{\mathrm{GF}} > 1.6$ (5.18)

It is interesting to compare the MRF obtained by additionally using the R_{GF} parameter to that obtained when only using the standard cut variables (Λ, β and reconstructed energy). When comparing the results from section 5.3.1 to the results obtained in this section (for the increased atmospheric neutrino background) it is found that the MRF is 1.4% better when additionally using the R_{GF} parameter. In addition, the expected number of signal events (from the Drift model) increases from 1.52 to 1.83 (i. e. a 20% increase).

5.3.4 *Additional optimisation*

In the cut optimisation described in the last sections, two simplifications have been used: the cut on the reconstructed zenith angle

ATM. ν		OPTIMAL CUT VALUES		MIN.			
FLUX	$\hat{\theta}$-CUT	Λ	$\log_{10}(E_{\mathrm{rec}})$	MRF	μ_{s}	μ_{b}	PURITY
Default	90°	−5.59	2.55 (= 355 GeV)	12.60	1.76	129	91.5%
	87°	−5.62	2.55 (= 355 GeV)	12.64	1.81	137	89.4%
	84°	−5.58	2.55 (= 355 GeV)	12.63	1.75	129	91.2%
	81°	−5.53	2.55 (= 355 GeV)	12.95	1.69	126	88.7%
25% incr.	90°	−5.62	2.55 (= 355 GeV)	13.87	1.80	166	92.0%
	87°	−5.66	2.55 (= 355 GeV)	13.94	1.86	178	89.7%
	84°	−5.62	2.55 (= 355 GeV)	13.94	1.81	168	91.4%
	81°	−5.62	2.7 (= 501 GeV)	14.21	1.71	157	87.3%
25% decr.	90°	−5.55	2.6 (= 398 GeV)	11.12	1.69	91.1	90.7%
	87°	−5.55	2.55 (= 355 GeV)	11.19	1.71	94.8	90.0%
	84°	−5.52	2.55 (= 355 GeV)	11.18	1.67	90.4	91.3%
	81°	−5.53	2.55 (= 355 GeV)	11.51	1.69	97.8	85.4%

Table 5.9: Optimal cuts and obtained MRF value for the different cuts on the reconstructed zenith angle.

is fixed to 90° and the same cuts are applied regardless of which trigger algorithm selected the event. In this section the effect of these simplifications is investigated.

Relaxing the cut on the reconstructed zenith angle

In the standard optimisation, only events which are reconstructed as upgoing are considered. It could be beneficial to extend the zenith cut somewhat. The visibility of the Galactic centre (from where the highest signal is expected) is about 68% when considering only upgoing events (i. e. with $\hat{\theta} > 90°$). However, extending the cut on the reconstructed zenith to 81° for instance, the visibility rises to 77%.

From the $\cos\hat{\theta}$ distribution in figure 5.9 it can be seen that the atmospheric muon background remains constant until about $\cos\hat{\theta} = 0.15$ (which corresponds to $\hat{\theta} \simeq 81°$), so by retuning the Λ cut, it is possible that a better sensitivity is obtained.

In order to check this, the R_{GF} and β cuts are fixed at the values found in the previous section and zenith cuts of 81°, 84°, 87° and 90° are tested. In each case the $\log_{10}(E_{\mathrm{rec}})$ and Λ cuts are optimised, where the cut on Λ is varied between -5.7 and -5.45 in steps of 0.01. Note that the step size in Λ is now 4 times as fine as before.

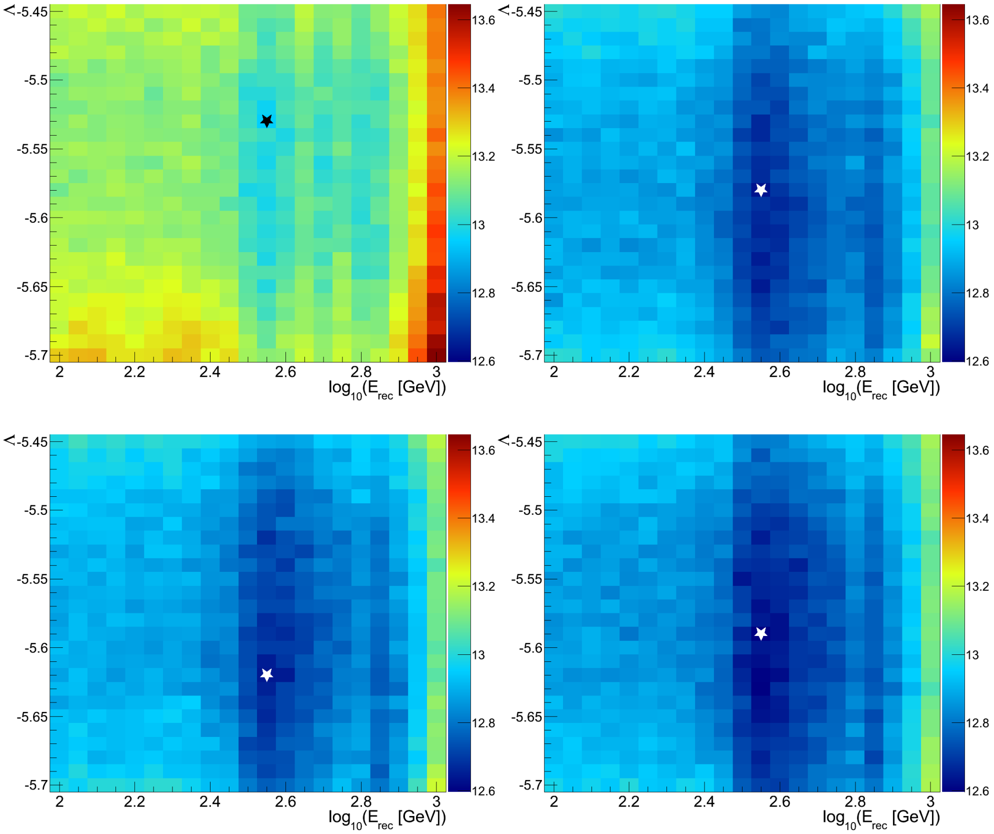

Figure 5.15: MRF versus Λ and $\log_{10}(E_{\text{rec}})$. The white (black) star marks the location of the minimum. TOP LEFT: for $\hat{\theta} > 81°$. TOP RIGHT: for $\hat{\theta} > 84°$. BOTTOM LEFT: for $\hat{\theta} > 87°$. BOTTOM RIGHT: for $\hat{\theta} > 90°$.

The results are summarised in table 5.9 and the MRF is plotted versus Λ and $\log_{10}(E_{\text{rec}})$ for each of the $\hat{\theta}$ cuts in figure 5.15. It can be seen that relaxing the cut on the reconstructed zenith angle does not result in a much better value for the MRF. Relaxing the zenith cut to 87° increases the signal a bit, but the background increases also, due to the slightly looser Λ cut found to be optimal in this case. The resulting purity of the final event sample is then lower, and a worse MRF value is found compared to a zenith cut of 90°. Relaxing the zenith cut to 84° gives almost the same results as for the zenith cut at 90°. The signal is slightly lower in this case, again resulting in a slightly higher MRF value. When relaxing the zenith cut to 81°, the MRF gets significantly worse.

In conclusion, relaxing the zenith cut is not beneficial, so the default cut ($\hat{\theta} > 90°$) is kept. Since a finer step size is used for the Λ parameter, a slightly different optimal value is found for this parameter. This value will be used instead of the one found in the standard optimisation. As before, the cuts obtained for the increased atmospheric neutrino background are chosen, resulting in the same cuts as listed in equation 5.18, with the difference that $\Lambda > -5.62$ instead.

Retuning the cuts for events only triggered by the TQ trigger

Finally, it is checked if separately optimising the cuts for events triggered only by the TQ trigger is beneficial. This concerns events that are triggered exclusively by the TQ trigger and not by the 3N or 2T3 triggers. These events will be referred to as *TQonly* events. Until now the same cuts have been applied to all events. For the optimal cut combination, the TQ trigger adds about 1% more neutrinos, and by retuning the cuts on the TQonly events this percentage might increase.

To check this, the cuts on the events triggered by the 3N and/or 2T3 triggers are kept fixed at the values found in the previous section and the cuts for events only triggered by the TQ trigger are varied. In this, only the Λ and $\log_{10}(E_{\text{rec}})$ cuts are varied; the β and R_{GF} cuts are kept fixed. The cut on the logarithm of the reconstructed energy is, as before, varied between 2.0 and 3.0 in steps of 0.05 and the cut on Λ is varied between -5.7 and -5.45 in steps of 0.01.

The results for varying the cuts on the TQonly events and keeping them fixed to the cuts found in the last section are summarised in table 5.10. The MRF versus Λ and $\log_{10}(E_{\text{rec}})$

ATM. ν FLUX	TQONLY CUTS	OPTIMAL CUT VALUES Λ	$\log_{10}(E_{\text{rec}})$	MIN. MRF	μ_{s}	μ_{b}	PURITY
Default	Fixed	-5.62	2.55 (= 355 GeV)	12.60	1.80	135	90.2%
	Varied	-5.47	2.35 (= 224 GeV)	12.54	1.80	134	90.6%
25% incr.	Fixed	-5.62	2.55 (= 355 GeV)	13.87	1.80	166	92.0%
	Varied	-5.57	2.4 (= 251 GeV)	13.84	1.80	165	92.4%
25% decr.	Fixed	-5.62	2.55 (= 355 GeV)	11.18	1.80	105	87.3%
	Varied	-5.46	2.2 (= 158 GeV)	11.09	1.80	104	87.9%

Table 5.10: Optimal cuts and obtained MRF value when retuning the cuts on TQonly events.

for an increased atmospheric neutrino background is shown in figure 5.16. Note that the maximum MRF value in the plot is only 2.5% higher than the minimum, so the variations are very small. The MRF improves slightly by retuning the cuts for the TQonly events, which is caused by an increase of the purity of the sample. The table confirms the main conclusion. The sample of events exclusively triggered by the TQ trigger has a slightly higher contamination of misreconstructed atmospheric muons, so by applying a slightly stricter Λ cut on these events, the signal is kept constant while the background is decreased. The effect is small because the livetime of the TQ trigger is 0.66 year compared to the total livetime of 3.53 year.

Even though the effect of applying different cuts to the TQonly events is small, it does provide a lower MRF value and the expected background decreases by about 1 event. So, for the final event selection, all events are selected that pass the following set of cuts:

- $\cos\hat{\theta} < 0$
- $\beta < 8.0°$
- $R_{\mathrm{GF}} > 1.6$
- For 3N or 2T3 triggered events:
  - $\Lambda > -5.62$
  - $\log_{10}(E_{\mathrm{rec}}) > 2.55$
- For TQonly triggered events:
  - $\Lambda > -5.57$
  - $\log_{10}(E_{\mathrm{rec}}) > 2.4$ (5.19)

To check the effect of including events triggered by the TQ trigger, the results obtained above are compared to the results obtained when only using the events triggered by the 3N and/or the 2T3 trigger. Not including the TQonly events[30] gives $\mu_{\mathrm{s}} = 1.74$ and $\mu_{\mathrm{b}} = 156$, resulting in a MRF of 13.92. Comparing these numbers to the results obtained above shows that that the MRF improves by 0.6% when including the TQ triggered events and 3% more signal events are expected from the Drift model.

The increase in the signal of 3% can be compared with the expected gain for the diffuse Galactic neutrino flux of 6%, as calculated in section 4.2.4. The quoted gain of 6% is at trigger level however, whereas not all of the extra neutrinos are reconstructable and/or pass the applied quality cuts, which explains the difference. In addition, since the background increases as

---

[30] *The cuts are re-optimised for the sample without the TQ triggered events, resulting in:* $R_{GF} > 1.6$, $\beta < 8.0°$, $\Lambda > -5.63$, $\log_{10}(E_{rec}) > 2.65$.

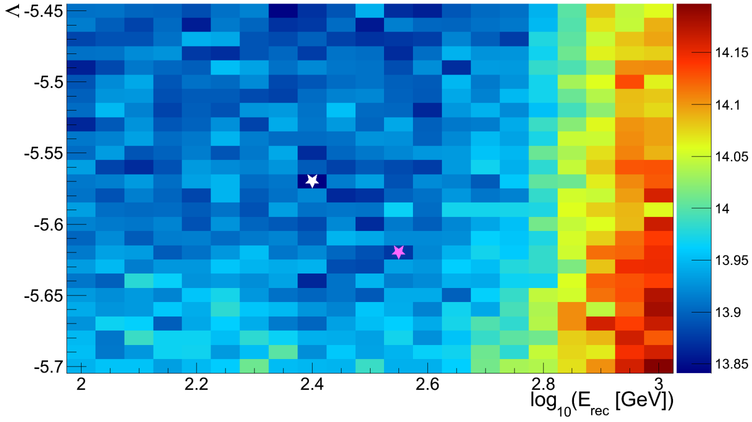

Figure 5.16: MRF versus Λ and $\log_{10}(E_{\text{rec}})$ for an increased atmospheric neutrino background. The white star marks the location of the minimum when retuning the cuts on the TQonly triggered events; the purple star marks the location of the minimum when keeping the cuts fixed to the optimal values found in the previous section.

well, the improvement in sensitivity is only 0.6%. Nevertheless, using the TQ trigger is beneficial.

5.4 ANTARES SENSITIVITY

After the final event sample has been obtained, the sensitivity of ANTARES to the diffuse Galactic neutrino flux can be determined. For this, the data from the background regions are used. The number of events surviving the cuts in each of the 8 background regions is presented in table 5.11. The distribution of the events is shown in figure 5.19; for the numbering of the regions see figure 5.5.

The background measurement gives an expected background of $n_{\text{b}} = 166 \pm 5$, which can be used to calculate the MRF for the four signal models. Since the background measurement has been performed, the average signal upper limit is calculated slightly different than given by equation 5.5, since no averaging has to be performed over the possible values of n_{bg} and n_{b} will be used instead of μ_{b}:

$$\bar{\mu}^{\alpha}(n_{\text{obs}}, n_{\text{bg}}) = \sum_{n_{\text{obs}}=0}^{\infty} \mu^{\alpha}(n_{\text{obs}}, n_{\text{bg}}) \frac{n_{\text{b}}^{n_{\text{obs}}} e^{-n_{\text{b}}}}{n_{\text{obs}}!}, \tag{5.20}$$

which will be used in equation 5.6.

BACKGROUND	NUMBER OF EVENTS		
REGION	3N + 2T3	TQONLY	TOTAL
1	161 ± 13	2 ± 2	163 ± 13
2	165 ± 13	2 ± 2	167 ± 13
3	174 ± 13	3 ± 2	177 ± 14
4	147 ± 12	2 ± 2	149 ± 12
5	141 ± 12	3 ± 2	144 ± 12
6	162 ± 13	1 ± 1	163 ± 13
7	177 ± 13	3 ± 2	180 ± 13
8	178 ± 13	3 ± 2	181 ± 13
Sum	1305 ± 36	19 ± 4	1324 ± 36

Table 5.11: Number of events measured per background region. The error on the number of events is the statistical uncertainty.

Table 5.12 summarises the expected signal and average MRF values for the four signal models. Also shown is the energy validity range of the average upper limit, which is defined to be the energy interval containing the central 90% of the detected signal[31].

			ENERGY
MODEL NAME	μ_S	MRF	VALIDITY RANGE
NoDrift_simple	0.90	27.57	0.17 TeV – 61 TeV
NoDrift_advanced	1.12	22.11	0.15 TeV – 45 TeV
Drift	1.80	13.77	0.18 TeV – 66 TeV
Fermi $\gamma \rightarrow \nu$	1.41	17.65	0.18 TeV – 71 TeV

Table 5.12: Expected signal, MRF and energy validity range for the signal models.

For the Drift model, the obtained MRF is 13.77, which is slightly lower than the MRF obtained for this cut combination in the previous chapter. This is caused by the different way of calculating the average signal upper limit.

The signal predictions for the other three models are lower, resulting in a higher MRF value. Also the energy validity ranges are slightly different, which is caused by a different predicted spectral index of the signal, see also table 2.3.

[31] *The energy validity range is determined using the MC simulation.*

The sensitivity can also be presented in a model independent way, by starting with an isotropic flux with a given spectral index γ and an arbitrary normalisation given by the flux constant $\mathcal{F}_\gamma$:

$$\Phi_{\nu_\mu+\overline{\nu}_\mu} = \mathcal{F}_\gamma \cdot E_\nu^{-\gamma}\,\mathrm{GeV}^{-1}\,\mathrm{m}^{-2}\,\mathrm{sr}^{-1}\,\mathrm{s}^{-1}, \tag{5.21}$$

and calculating the average expected flux upper limit $\overline{\mathcal{F}}_\gamma^{90\%}$ (at a confidence level of 90%). The advantage of presenting the sensitivity in this way, is that it is more general, and not just applicable to a single signal model.

SPECTRAL INDEX	$\overline{\mathcal{F}}_\gamma^{90\%}$	ENERGY VALIDITY RANGE
2.5	$1.4\,\mathrm{GeV}^{1.5}\,\mathrm{m}^{-2}\,\mathrm{sr}^{-1}\,\mathrm{s}^{-1}$	0.24 TeV – 96 TeV
2.6	$3.2\,\mathrm{GeV}^{1.6}\,\mathrm{m}^{-2}\,\mathrm{sr}^{-1}\,\mathrm{s}^{-1}$	0.18 TeV – 71 TeV
2.7	$7.1\,\mathrm{GeV}^{1.7}\,\mathrm{m}^{-2}\,\mathrm{sr}^{-1}\,\mathrm{s}^{-1}$	0.15 TeV – 52 TeV

Table 5.13: The average limit on the flux constant for different values of γ.

The spectral indices predicted by the signal models are in the range from 2.6 and 2.7, so the sensitivity is calculated for these two values of γ. Besides these values, the sensitivity is also calculated for $\gamma = 2.5$. The results are shown in table 5.13.

The sensitivity for $\gamma = 2.7$ can be compared to the flux upper limit as set by the AMANDA-II experiment:

$$\Phi_{\nu_\mu+\overline{\nu}_\mu} < 4.8\,E_\nu^{-2.7}\,\mathrm{GeV}^{-1}\,\mathrm{m}^{-2}\,\mathrm{sr}^{-1}\,\mathrm{s}^{-1}, \tag{5.22}$$

with E_ν in GeV, which is valid in the energy range from 0.2 TeV to 40 TeV [Kelley et al., 2005]. By comparing the normalisation factor to the corresponding result in table 5.13 it can be seen that the ANTARES sensitivity is about 50% worse than this limit.

However for a fair comparison the ANTARES sensitivity should be compared to the AMANDA-II sensitivity. In the AMANDA-II analysis 283.3 background events were expected, but the data in the signal region underfluctuated and only 272 events were observed. Using the expected number of background events gives a sensitivity of $7.8\,\mathrm{GeV}^{1.7}\,\mathrm{m}^{-2}\,\mathrm{sr}^{-1}\,\mathrm{s}^{-1}$, which is 10% worse than the ANTARES sensitivity. Also the energy validity range of the AMANDA-II limit is slightly smaller.

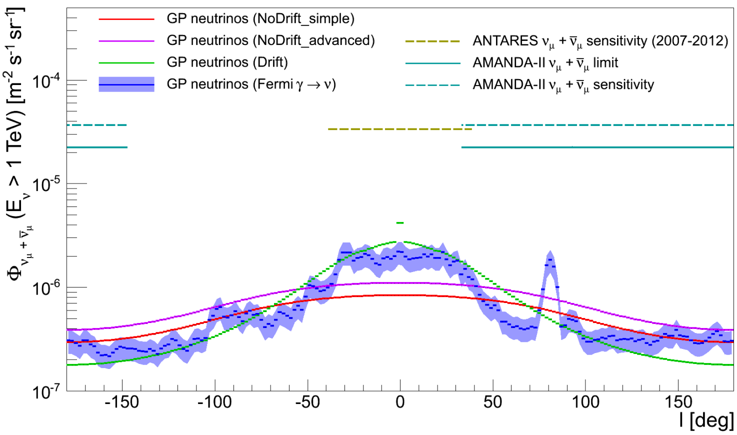

Figure 5.17: Sensitivities and AMANDA-II limit versus Galactic longitude together with the average signal fluxes ($|b| < 4.5°$) above 1 TeV.

The AMANDA-II limit and the sensitivities for both experiments are shown versus Galactic longitude in figure 5.17, together with the average signal fluxes from the four models (as already shown on a linear scale in figure 2.25). This plot shows a more important difference between the two experiments. A different region has been used as signal region by the AMANDA-II experiment: $33° < l < 213°$ and $-4.4° < b < 4.4°$. While the latitudinal extension of this signal region has been optimised using the MRF method, the longitudinal extension has been chosen simply because this is the range of longitude values AMANDA-II can observe (around $b = 0°$), see also figure 2.28. The size of the signal region used by AMANDA-II is 0.48 sr, which is a factor of about 2.3 bigger than that used in the ANTARES analysis. Since a bigger region is used by AMANDA-II, the sensitivity will be lower. To really compare the sensitivities, one should consider how they compare to the expected signal fluxes in both regions. The average fluxes in the signal region used by AMANDA-II are on average a factor of about three lower than the fluxes in the signal region used in the ANTARES analysis (see also table 2.3), making the ANTARES sensitivity a factor of three more stringent.

5.4.1 *The cosmic neutrino flux measured by IceCube*

As mentioned already in the introduction, the IceCube experiment has recently measured a flux of cosmic neutrinos. At the time of writing, the flux seems isotropic. The most recent publication by IceCube [Aartsen et al., 2015] gives the following parameterisation of the flux (per neutrino flavour):

$$\Phi_{\nu+\bar{\nu}} = 2.06^{+0.4}_{-0.3} \cdot 10^{-14} \left(\frac{E_\nu}{10^5\,\mathrm{GeV}} \right)^{-2.46\pm0.12} \mathrm{GeV}^{-1}\,\mathrm{m}^{-2}\,\mathrm{sr}^{-1}\,\mathrm{s}^{-1}. \tag{5.23}$$

Using the best-fit results (i. e. the mean of the two fit parameters) for the flux given by equation 5.23 and assuming the flux is truly diffuse, 1.0 event is expected from this flux in the signal region for the livetime considered here. In case of a diffuse flux, the same number of events is expected also in each of the background regions, so the sensitivity to an additional flux of neutrinos from the Galactic plane is not affected (since the background is measured from data). If however, the flux is Galactic in origin (or has a significant Galactic component), there will be an additional contribution to the number of events in the signal region, which could show up as an excess.

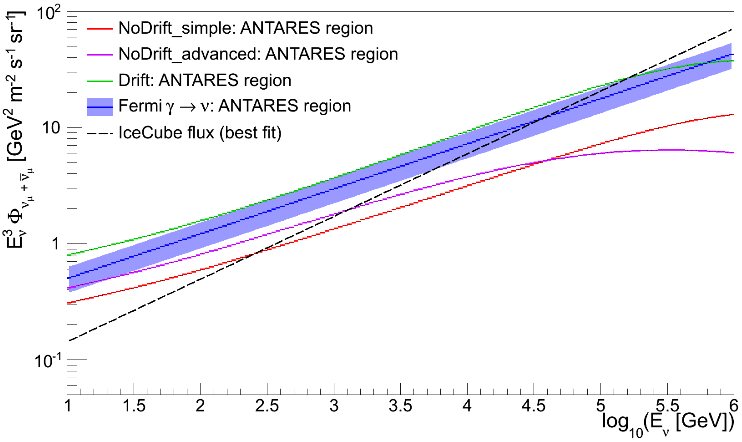

Figure 5.18: Average diffuse Galactic neutrino fluxes in the ANTARES signal region together with the best-fit to the flux measured by IceCube versus neutrino energy.

It is interesting that the number of events expected in the signal region is of the same order as the signal predicted by the four diffuse Galactic neutrino flux models that are used (which ranges from 0.9 to 1.8). This is not surprising, since the IceCube flux is comparable in size to the average fluxes predicted in the signal region, as can be seen from figure 5.18 in which the fluxes are plotted versus neutrino energy. In addition, the best-fit value for the spectral index is 2.46, which is close to the spectral indices predicted by the models (2.6 to 2.7).

From figure 5.18 it seems that the neutrino flux measured by IceCube could be explained as being from cosmic rays interacting in our Galaxy. However, one should keep in mind that the diffuse Galactic neutrino fluxes that are shown in the figure are the average fluxes in the ANTARES signal region, while the IceCube flux is an isotropic flux. Assuming that the fluxes are isotropic and comparing the neutrino fluxes integrated over the full sky leads to the conclusion that the flux observed by IceCube is between one and two orders of magnitude higher. This means that the flux measured by IceCube cannot be explained as originating solely from cosmic ray interactions with interstellar matter in our Galaxy.

5.5 RESULTS

The background measurement described earlier gives an expected background of $n_{\mathrm{b}} = 166 \pm 5$. In the signal region a total of $n_{\mathrm{obs}} = 177 \pm 13$ events are measured. This number consists of 176 events triggered by the 3N and/or 2T3 triggers and 1 event triggered exclusively by the TQ trigger. A sky-map of the event distribution is shown in figure 5.19.

Figures 5.20 and 5.21 show Data-MC comparison plots for the reconstructed zenith and azimuth angles ($\hat{\theta}$ and $\hat{\phi}$ respectively) and the four quality parameters: Λ, β, E_{rec} and R_{GF}. The left plots in these figures show the distributions for events that are reconstructed in the background regions; the right plots show the same for events reconstructed in the signal region. Like in figure 5.9, the data (in black) is compared to the atmospheric muon simulation (in red) and the atmospheric CC muon (anti-) neutrino simulation (in purple); in addition the fluxes predicted by the Drift and Fermi $\gamma \rightarrow \nu$ models are shown. For each of the plots all cuts shown in equation 5.19 are applied, except the cut on the variable that is plotted (if applicable)[32]. The cut is represented by the dashed dark blue line. In addition, the ratio of data to the sum of the MC contributions is calculated and shown below the corresponding figure; the red line in this plot denotes a ratio of 1.

When comparing the distributions for signal and background regions, it can be seen that the shape is the same. The data and atmospheric neutrino fluxes are about 8 times as high in the background regions, whereas the signal predicted by the Drift and Fermi $\gamma \rightarrow \nu$ models is higher in the signal region. This is expected, since the signal region is defined to maximise the sensitivity and there are 8 background regions.

[32] *Since different Λ and $\log_{10}(E_{rec})$ cuts are obtained for events triggered by the 3N and/or 2T3 triggers as for TQonly events, the cuts on these parameters are not shown.*

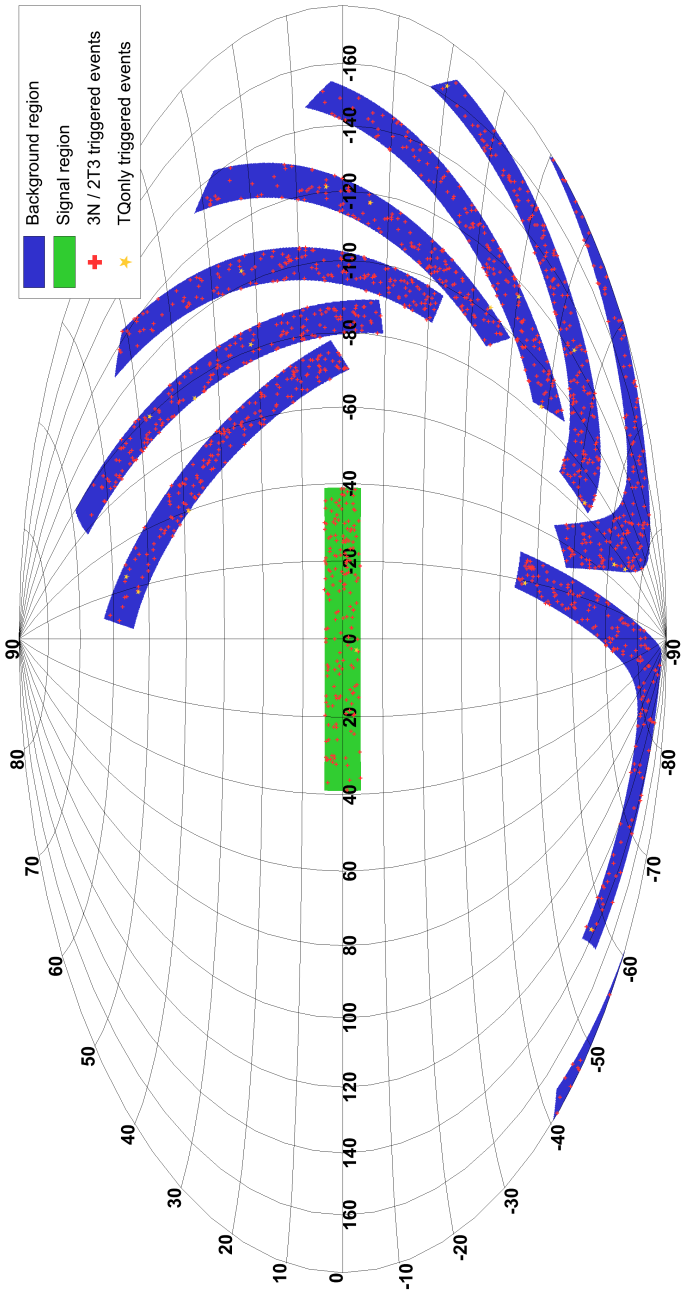

Figure 5.19: The distribution of the events in the signal region and the 8 background regions.

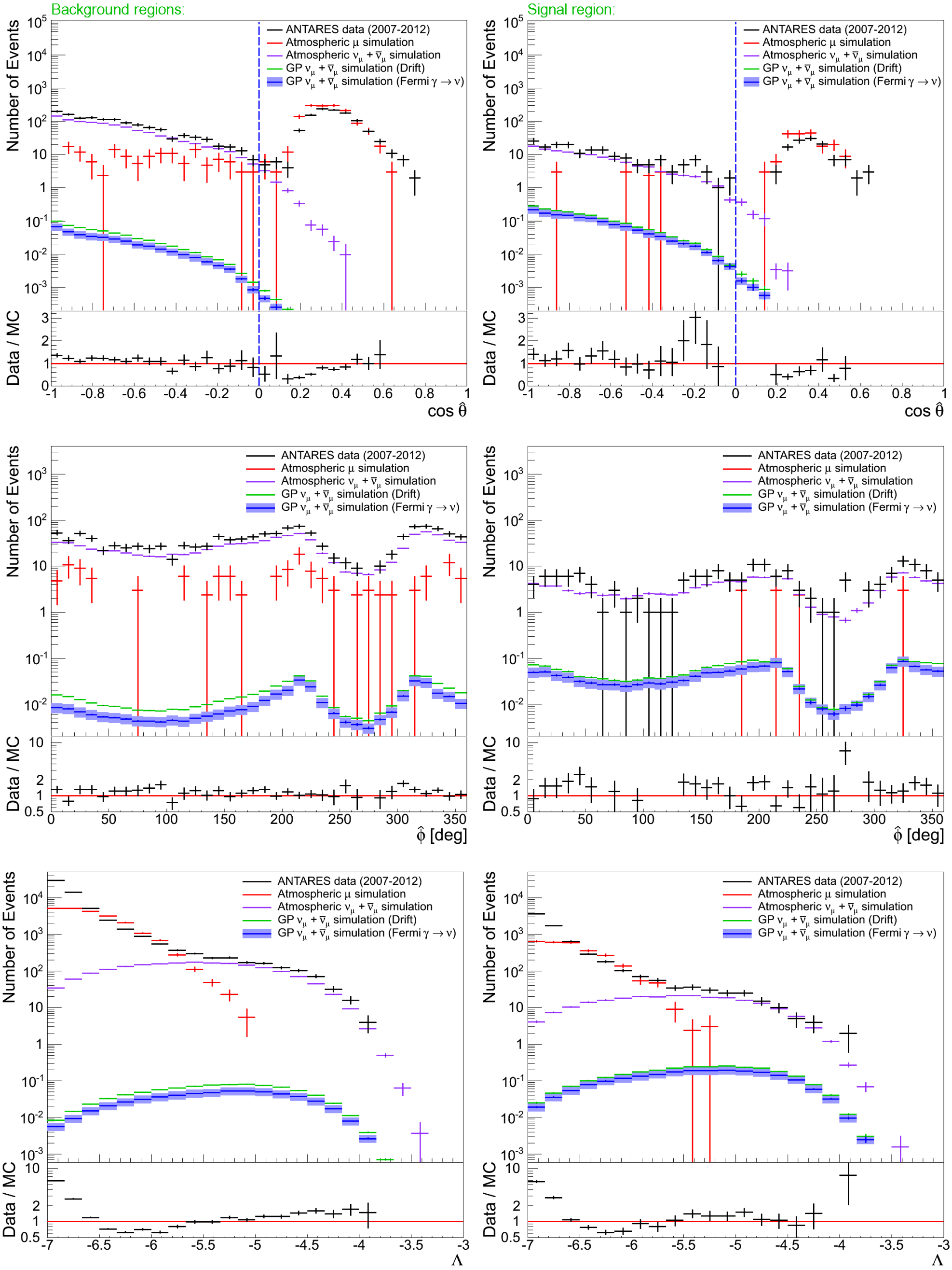

Figure 5.20: Data-MC comparison plots for events from the background regions (left plots) and from the signal region (right plots). TOP ROW: $\cos\hat{\theta}$ distributions. MIDDLE ROW: reconstructed azimuth angle distributions. BOTTOM ROW: Λ distributions.

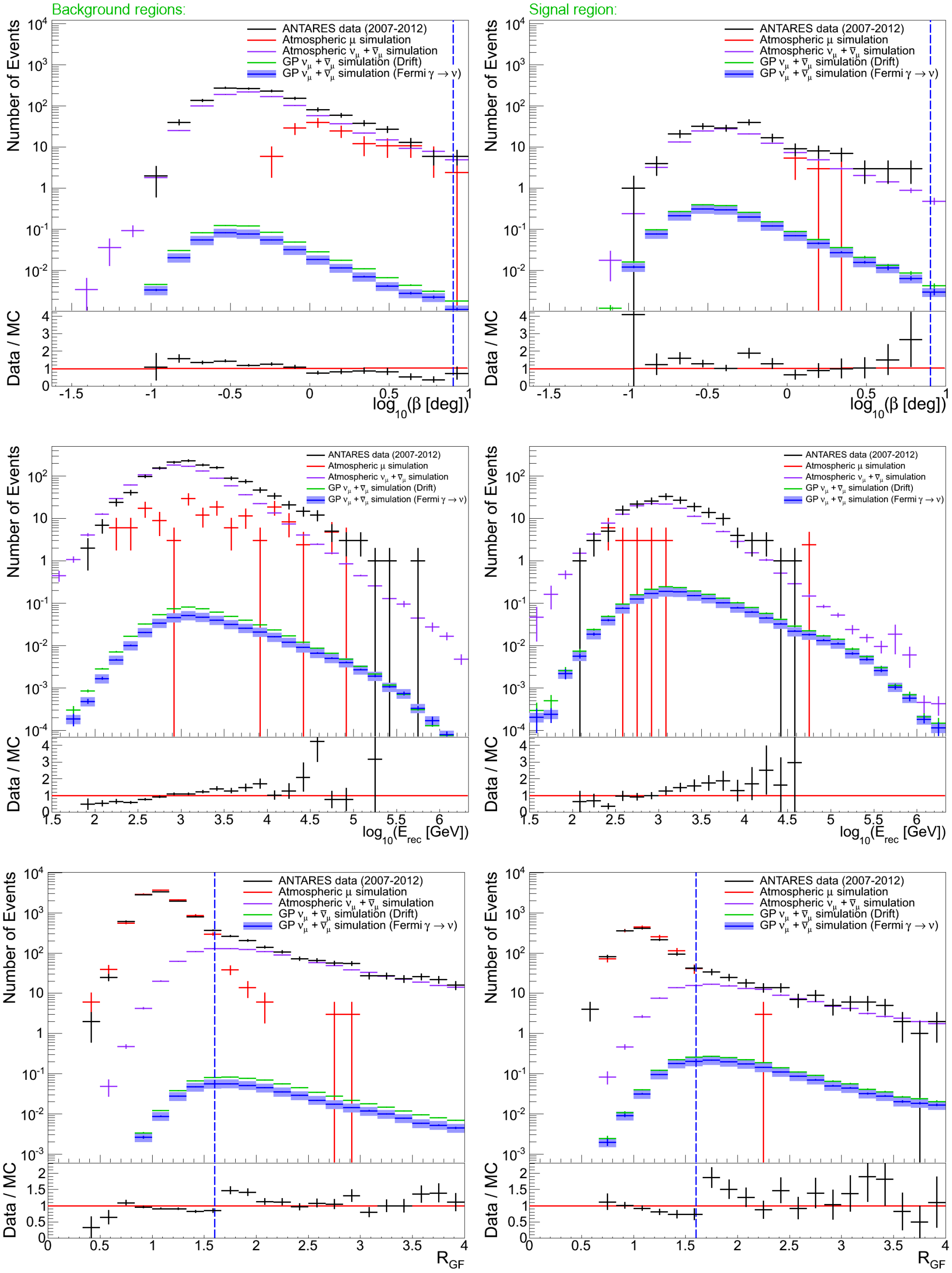

Figure 5.21: Data-MC comparison plots for events from the background regions (left plots) and from the signal region (right plots). TOP ROW: β distributions. MIDDLE ROW: $\log_{10}(E_{\text{rec}})$ distributions. BOTTOM ROW: R_{GF} distributions.

The measured number of events corresponds to a slight over-fluctuation, with a significance given by [Li and Ma, 1983]:

$$S = \sqrt{2n_{\text{obs}} \ln\left[(\tau+1)\frac{n_{\text{obs}}}{n_{\text{obs}}+\tau\, n_{\text{b}}}\right] + 2\tau\, n_{\text{b}} \ln\left[(\tau+1)\frac{n_{\text{b}}}{n_{\text{obs}}+\tau\, n_{\text{b}}}\right]}, \tag{5.24}$$

which gives $S = 0.8\sigma$. From this it can be concluded that the excess is not significant and the measurement is compatible with the background expectation.

SPECTRAL INDEX	$\mathcal{F}_{\gamma}^{90\%}$	ENERGY VALIDITY RANGE
2.5	$2.0\,\mathrm{GeV}^{1.5}\,\mathrm{m}^{-2}\,\mathrm{sr}^{-1}\,\mathrm{s}^{-1}$	0.24 TeV – 96 TeV
2.6	$4.6\,\mathrm{GeV}^{1.6}\,\mathrm{m}^{-2}\,\mathrm{sr}^{-1}\,\mathrm{s}^{-1}$	0.18 TeV – 71 TeV
2.7	$10\,\mathrm{GeV}^{1.7}\,\mathrm{m}^{-2}\,\mathrm{sr}^{-1}\,\mathrm{s}^{-1}$	0.15 TeV – 52 TeV

Table 5.14: The obtained limit on the flux constant for different values of γ.

Since no significant excess has been observed, the observed number of events can be converted into a flux upper limit. The limits that can be set are shown in table 5.14. These limits are above the sensitivities shown in table 5.13 since more events are measured in the signal region than expected from the background-only hypothesis.

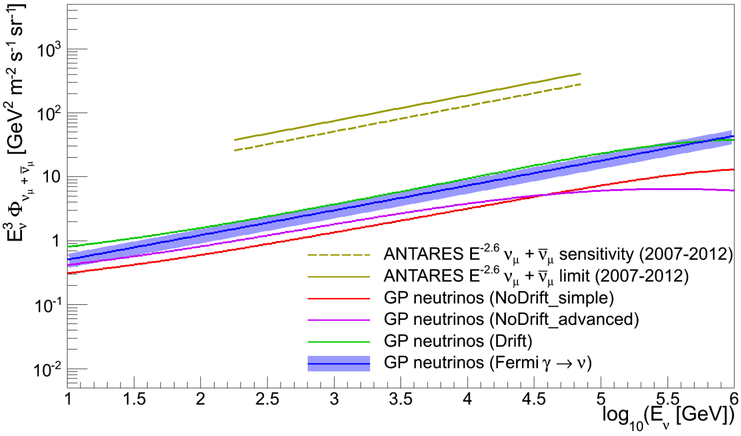

Figure 5.22: ANTARES limit and sensitivity versus neutrino energy for $\gamma = 2.6$ together with the average fluxes from the four signal models.

The flux upper limit, for a spectral index of $\gamma = 2.6$ is shown versus neutrino energy in figure 5.22, together with the sensitivity and the average signal fluxes from the four models. The flux upper limit is a factor of about 20 above the flux predicted by the Drift model and a factor of about 25 above the Fermi $\gamma \rightarrow \nu$ model predictions.

The flux upper limit versus Galactic longitude is shown in figure 5.23, where the limit and sensitivity are shown for a spectral index of $\gamma = 2.7$. The ANTARES limit is a factor of 2.1 above the limit set by AMANDA-II. As explained in the previous section, this is caused by an underfluctuation in the AMANDA-II measurement and an overfluctuation in the ANTARES measurement. It should be stressed however, that different signal regions are used, and that the limit obtained here is the first of its kind covering the inner Galactic plane region.

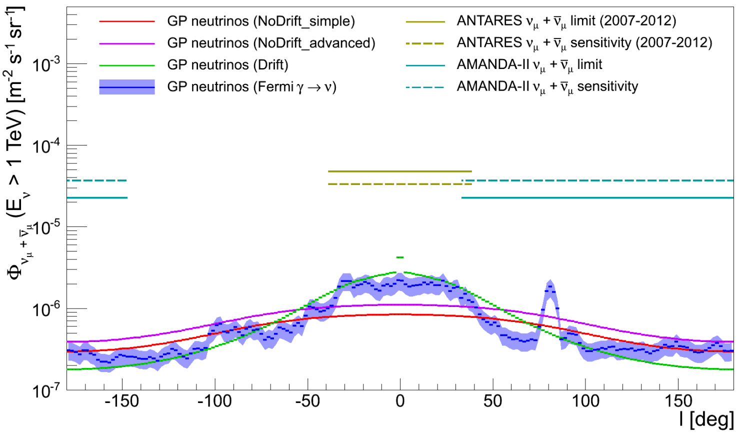

Figure 5.23: Sensitivities and limits versus Galactic longitude together with the average signal fluxes ($|b| < 4.5°$) above 1 TeV.

Even though the expected fluxes in the signal region are higher and the sensitivity of ANTARES is better than that of AMANDA-II, the sensitivity is still more than a factor of 10 higher than even the most optimistic signal flux model. From this it can be concluded that a bigger neutrino telescope, like KM3NeT, is needed to constrain the models further and learn more about the diffuse Galactic neutrino flux. The sensitivity of KM3NeT will be assessed in the next chapter.

Before turning to KM3NeT, some more information is extracted from the flux upper limits, which can also be used to say something about the origin of the flux measured by IceCube. One can test the hypothesis that all the events measured by

IceCube originate from the signal region used in this analysis ($-39° \leqslant l \leqslant +39°$ and $-4.5° \leqslant b \leqslant +4.5°$). Since the signal region takes up only 1.7% of the total sky, the flux from this region has to be a factor of about 60 more intense than the diffuse flux from equation 5.23 to result in the same number of observed events for IceCube [Spurio, 2014]:

$$\Phi_{\nu+\bar{\nu}} = 3.8^{+0.7}_{-0.6}\, E_\nu^{-2.5}\, \mathrm{GeV}^{-1}\, \mathrm{m}^{-2}\, \mathrm{sr}^{-1}\, \mathrm{s}^{-1}, \qquad (5.25)$$

for a spectral index of 2.5 and with E_ν in GeV.

Comparing this flux to the ANTARES 90% confidence level flux upper limit for the same spectral index shows that the limit is a factor of about 1.9 lower than this flux. The hypothesis that all events measured by IceCube originate from the signal region can thus be rejected. Furthermore, the limit indicates that at most about 50% of the flux measured by IceCube could originate from the signal region considered here.